High resolution tidal model of Canadian Arctic Archipelago, Baffin and Hudson Bay

Kleptsova, O.; Pietrzak, J. D.

DOI
10.1016/j.ocemod.2018.06.001

Publication date
2018

Document Version
Accepted author manuscript

Published in
Ocean Modelling

High resolution tidal model of Canadian Arctic Archipelago, Baffin and Hudson Bay

O. Kleptsova[a,*], J.D. Pietrzak[a]

[a] *Faculty of Civil Engineering and Geosciences, Delft University of Technology, Stevinweg 1, 2628CN Delft, The Netherlands*

Abstract

Ice induced variability of tides in the Canadian Arctic Archipelago, including Baffin Bay and Hudson Strait/Hudson Bay system, was studied by means of a new high resolution tidal model. Here we show that the seasonal variations of the tidal constants are significant in the major part of the domain. Month to month changes of the tidal phases can reach 180 degrees due to changes in the number and positions of the amphidromic points, whereas the amplitude variations are especially large in the near resonant basins. We also show that the tidal seasonality has undergone dramatic changes in the past decades due the decaying extent of the Arctic sea ice. These seasonal/decadal scale changes not only vary tidal dissipation on the shelf, but also impact tides in the adjacent open ocean and, therefore, cannot be neglected.

Keywords: Canadian Arctic Archipelago, tide, ocean modeling, sea ice, unstructured mesh, seasonal variation, Arctic ocean

1. Introduction

The Canadian Arctic Archipelago, shown in Figure 1, is a collection of islands located on the northern North American continental shelf. It is known to be an important gateway for water, ice and tidal energy exchange between the Arctic Ocean and North Atlantic. Changes in the circulation of freshened seawater and ice through its narrow passages have the potential to influence both regional and global climate. It can significantly affect the distribution of sea-ice in the Arctic, recirculation of the surface waters and freshwater fluxes around Greenland as well as the strength of ocean circulation in the Atlantic, Joyce and Proshutinsky (2007).

Accurate tide prediction is crucial for many purposes such as investigating the variability of the sea surface currents and eddy activities. Tidal motion influences the turbulent mixing and heat anomalies required for polynya formation and, therefore, affects sea ice properties and distribution, Wang et al. (2003); Makinson et al. (2011).

*Corresponding author:
Email address: O.S.Kleptsova@TUDelft.nl (O. Kleptsova)

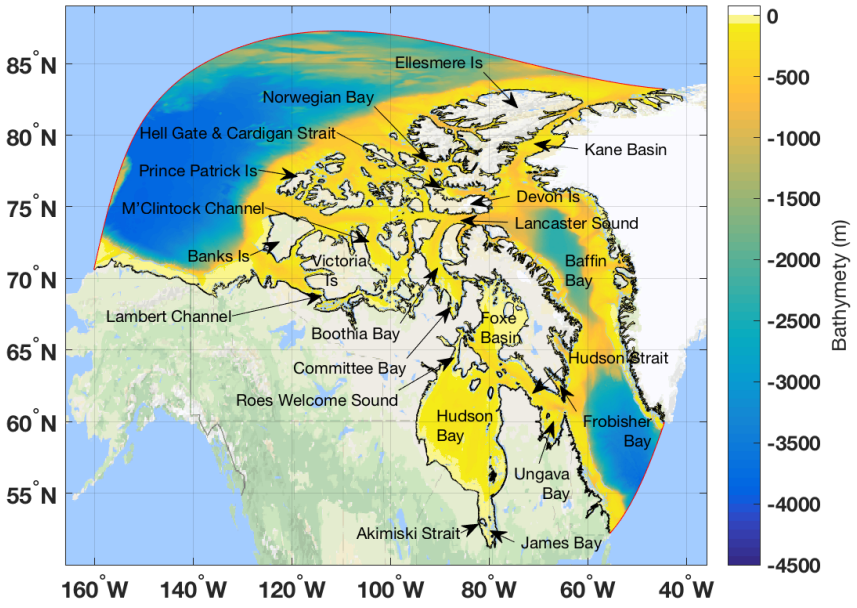

Figure 1: Model domain: bathymetry and shore lines.

Furevik and Foldvik (1996) have shown that near critical latitude the boundary layer thickens and it encompasses the entire water column at critical latitude. The thickened boundary layer imparts vertical shears in the horizontal velocities to more of the water column and can lead to mixing. As a result of the increased baroclinicity of the water column due to internal tides, enhanced mixing, resonant effects with the inertial frequency, even weak tidal regimes play a significant role in ice-shelf melting when they are subject to critical latitude effects, Robertson (2013).

While global ocean tide models improved dramatically in the recent years due to combination of data assimilation based on satellite altimetry analysis with sophisticated hydrodynamic/assimilation modeling, the accurate representation of shallow-water (depth $< 1000m$) and high-latitude (polewards from $\pm 66^{\circ}$) tides still remain a challenge, Cheng and Andersen (2011); Stammer et al. (2014). The model limitations in polar regions arise from a poorly known bathymetry and relatively sparse and poor quality data for model validation and assimilation. Another source of errors is the ice induced seasonal variability of the tidal constituents, which is insufficiently studied.

The existing tidal models represent an annual mean state of the tidal constants. The presence of ice cover and its effects are often ignored completely or represented via imposing a stationary mean ice concentration field. The rationale behind this is that the ice induced changes do not exceed the model errors. This conclusion is, however, drawn based only on a few tide gauge records along the White Sea coastline, off the Siberian continental shelf and in the Canadian Arctic, Henry and Foreman (1977); Murty and Polavarapu (1979); Godin and Barber (1980); Murty (1985); Prinsenberg (1988); St-Laurent et al. (2008). There is no data and there are only a few numerical

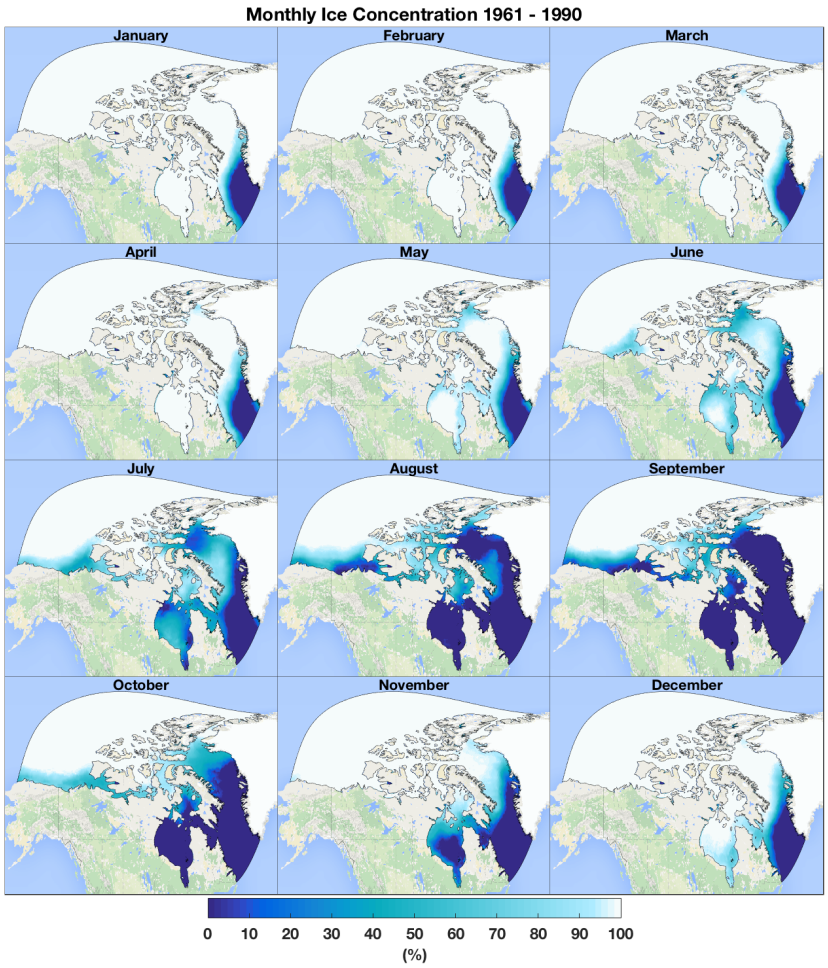

Figure 2: Monthly 1961-1990 median sea ice concentration, Walsh et al. (2015).

studies dedicated to the temporal variability of tidal constants on a larger scale, Kowalik (1981); Saucier et al. (2004); Kagan and Romanenkov (2007); Kagan et al. (2007); Kagan and Sofina (2010); Müller et al. (2014). The majority of the mentioned studies only compare winter and summer (January vs September) regimes. None of them show monthly variations of the tidal constituents and cover the complete area considered here.

In this paper a new tidal model of the Canadian Arctic Archipelago including Baffin Bay, Hudson Strait and Hudson Bay is developed and validated against available observations. The simulations were performed using ADCIRC unstructured model modified to account for the presence of an under-ice frictional layer. Unlike other existing models, the user defined ice concentration field used to calculate the ice-ocean drag coefficient is assumed to vary in time, Figure 2. Since the majority of the available tide

gauge records are too short to account for the tide seasonality, only a part of the simulated time series corresponding to the specific tidal record was used for comparison. After the inital model validation step, seasonality of the tidal constants in the entire domain was assessed by means of monthly harmonic analysis. The modelled variations were compared to the observations at a number of tide gauges with records spanning multiple years. The model behaviour in the Hudson Bay/Hudson Strait regions was also compared to the analytical model of the semi-diurnal response developed by Cummins et al. (2010). Although, the model does not account for a separate quarter-wavelength resonance exited at Leaf Basin in Ungava Bay, it gives a good indication of the range of semi-diurnal amplitude variation that can be expected in the resonant system due to the additional friction associated with the seasonal ice cover.

Estimates of M2 tidal energy dissipation from TOPEX/Poseidon altimeter data by Egbert and Ray (2001) has shown that the most important region of the world ocean for dissipating tidal energy is the area around Hudson Bay. High energy dissipation on a shelf is usually associated with tidal resonances. Indeed, results of Webb (2014) indicate that the Hudson Bay region has four significant resonances close to and straddling the semi-diurnal tidal band. Here we show that additional friction associated with the seasonally varying ice cover significantly influences tidal constants in the Hudson Bay region including Baffin Bay and Canadian Arctic straits. This, in turn, changes the amount of energy dissipated in the Hudson Bay and, thus, has potential to introduce seasonal variations of tides in the Northern Labrador Sea.

The paper is organized as follows: Section 2 gives a short description of ADCIRC including the implementation of the ice-ocean interation, design of the numerical experiment, observation data and error metrics used for the model validation. Model results are presented in Sections 3-5 and summarized in Section 6. Extended model validation results are given in Appendix.

2. Model description

2.1. Description of the numerical method

In this study we use a modified verstion of ADCIRC. ADCIRC (ADvanced CIRCulation), Luettich and Westerink (2004), a multi-scale, multi-physics coastal circulation model that is widely used for a range of modelling applications. The model runs on highly flexible, unstructured triangular meshes and is, therefore, highly scalable with linear performance scaling up to 16,000 cores, see e.g. Dietrich et al. (2012).

ADCIRC is a continuous-Galerkin, finite-element, shallow-water model, which utilizes the Generalized Wave Continuity Equation (GWCE) formulation to determine the water levels; velocities are obtained from the vertically integrated momentum equation. In order to account for the under-ice friction, a potential damping mechanism that dissipates tidal energy is the friction produced at the interface between the ice and the ocean, ADCIRC was modified as described below.

The ocean currents and sea ice interaction is usually represented through a simple quadratic stress proportional to the relative velocity between ice and water, Pease et al. (1983). Dissipation of long-wave energy under drifting ice is negligible. However, during high ice concentration periods ice plates are confined by shorelines and

their mobility is hampered. The relative velocity between the ice and the tidal current increases and the stress becomes significant.

A practical approach to simulate under-ice friction effect in a 2D model is combine the surface and bottom drag into a single friction parameter:

$$C_D = C_{D_{bot}} + C_{D_{surf}} \tag{1}$$

Similarly to Dunphy et al. (2005); Hannah et al. (2008); Collins et al. (2011) the ice-ocean drag coefficient $C_{D_{surf}}$ is computed based on the fractional sea ice coverage as

$$C_{D_{surf}} = C_{D_{ice}} max(0, 2(A - \frac{1}{2})) \tag{2}$$

where $C_{D_{ice}} = 1.8 * 10^{-2}$ and A is the fractional sea ice coverage at the node of interest. $C_{D_{surf}}$ is zero for $A < \frac{1}{2}$, since ice floes are believed to move freely along with the surface waters. The maximum value $C_{D_{surf}}$ at $A = 1$ accounts for increased friction due to the keel effect in ridged ice (Tang and Fissel (1991)).

Another important effect of ice cover is that it also acts as a barrier to the meteorological forcing of the water mass. Macklin (1983) and Pease et al. (1983) found that measurements of wind drag coefficients over first year sea ice typically yielded values that were significantly larger and varied less with wind speed than that predicted for open water. It is important to accont for the changes of wind drag coefficient due to presence of ice when modeling storm surges and the associated flooding. However, they are unlikely to have significant effect on the long term tidal constants, and are, therefore, not considered in this study.

2.2. Model domain

The size of the domain is determined not only by the complexity of geometry, but also by the tidal dynamics in the area. To ensure the correct development and propagation of tides open boundaries should be placed outside of the resonant basins and should not located near the tidal amphidromes. The chosen model domain and bathymetry is shown in Figure 1.

The bathymetric data were extracted from the version 3.0 of International Bathymetric Chart of the Arctic Ocean (IBCAO), Jakobsson et al. (2012), which includes new bathymetric data from a number of sources, such as the fishing vessels, US Navy submarines and research ships from various nations. For the areas south of 64°N not covered by IBCAO data set the bottom heights were drawn from the GEBCO 2014 grid, Weatherall et al. (2015).

The model grid was produced using GMSH grid generator by Geuzaine and Remacle (2009), which was modified by van Scheltinga et al. (2012) to allow for efficient meshing of highly irregular oceanic domains. The mesh has about 390 thousand nodes and 750 thousand triangular elements with resolution varying from approximately 300m to 10km.

2.3. Observation data

Over many years, Canada has carried out tidal recordings at many locations spead over the Arctic Archipelago. A number of tide gauges were operated for long periods

of time, however, the majority of observations were collected during short campaigns run in the late 1970s-80s and typically cover time intervals of 30 to 80 days. Since the installation of tidal instruments during the short summer season is often hindered by moving ice floes and bergs and the uncertainty of finding open water, the majority of short term tidal records have been collected using instruments deployed in the winter through the ice cover, Tait et al. (1986). Conditions suitable for operation usually occur in a two-month window between mid to late February and late April to early May, depending on latitude.

Most of the observed water level data are available for download from a digital data inventory at the Marine Environmental Data Service (MEDS) Fisheries and Oceans Canada. In order to provide broad spatial coverage, we chose to use records with length of at least 29 days. The tidal constituents were calculated from the water level time series using UTide package, Codiga (2011). Additionally, the tidal constants were extracted from Collins et al. (2011); Chen et al. (2009) and the Danish tidal office report (Farvandsvæsenet (2000)). Locations of the tide gauges used for model validation are depicted in the top panel of the Figure 3 and together with the record period (there known) are listed in the supplement.

The fact that the tide gauge data were aquired during different periods and that the majority of the records are very short and do not account for the tidal seasonality poses a problem for comparison with the model result. To overcome the difficulty, only a part of the simulated time series corresponding to a specific tidal record (the same length and season) was used for comparison during the model step. We believe, this approach also helps to eliminate possible errors associated with short record length.

Similarly to Collins et al. (2011), for the purpose of reporting statistics the Archipelago was divided into a number of regions based on the tidal range. The regions are defined in Table 1 and tide gauges belonging to different regions are shown in different colors in Figure 3. For evaluation of the tidal currents in the Central Arctic Archipelago, we use stations from Collins et al. (2011). Figure 3 shows approximate locations of the moorings.

ID	Region
BB&LN	Baffin Bay and Northern Labrador sea
AW	Arctic West : Amundsen Gulf and Victoria Island
AN	Arctic North : Ellesmere Island and Nares Strait
ANW	Arctic Northwest : Prince Patrick Island, Melville Island and Amund Ringnes Island
AC	Arctic Central : Barrow Strait, Lancaster Sound and Jones Sound
ASC	Arctic South Central : MClintock Channel and Somerset Island
ASE	Arctic Southeast : Baffin Island North
HS&FB	Hudson Strait, Frobisher Bay and Cumberland Sound
HB	Hudson Bay

Table 1: The names of the regions used to provide summary statistics

2.4. Simulation parameters and boundary settings

The simulation is forced by prescribing the tidal motion on the open boundaries. The amplitude and phases of the 8 major constituents were compiled from TPXO8v1-atlas and two versions of FES global tide models. The TPXO8v1-atlas is the current

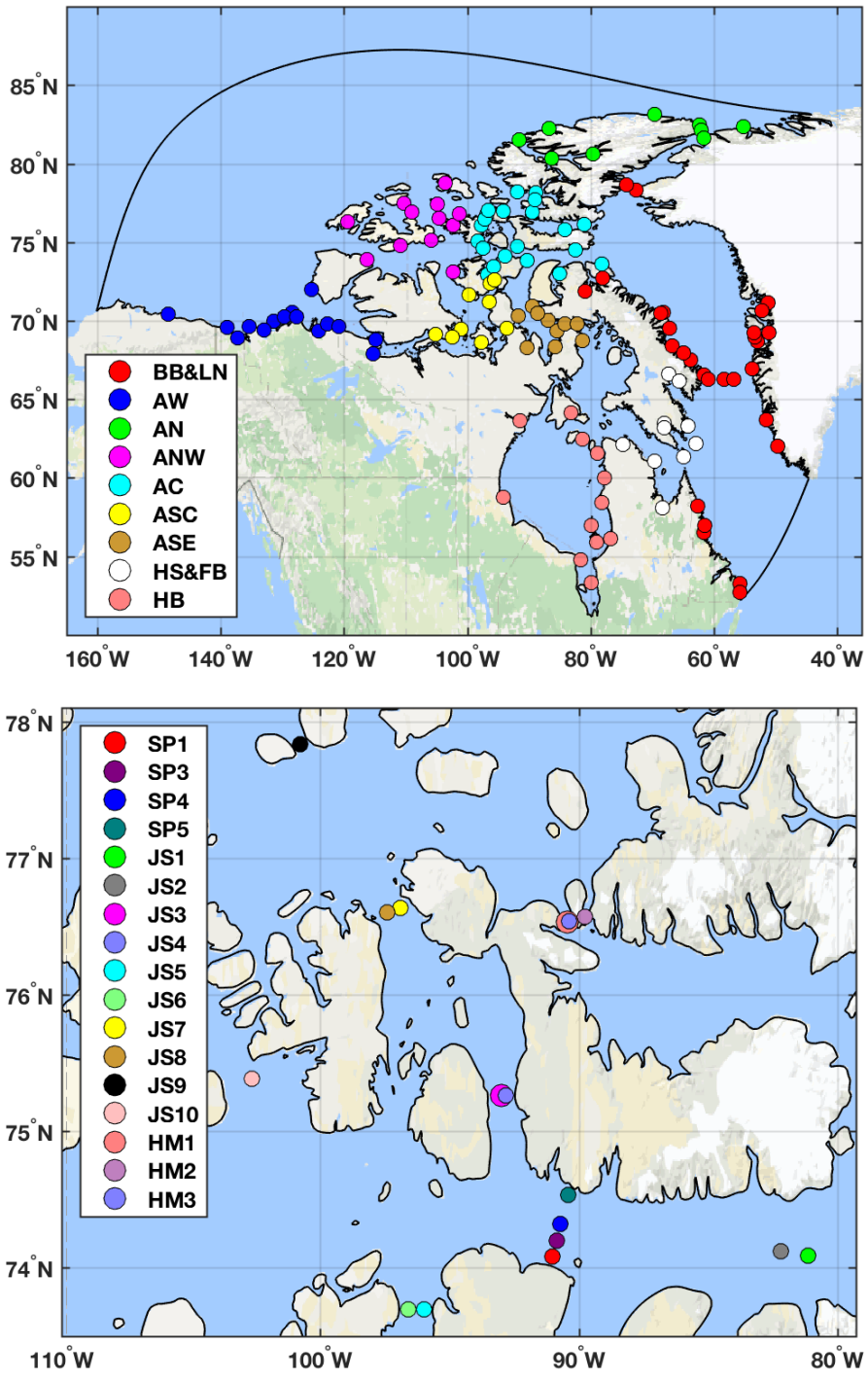

Figure 3: Approximate locations of the individual tide gauges color-coded according to the areas defined in Table 1 (top). Locations of the moorings in the Central Arctic Archipelago (bottom).

version of a global model of ocean tides obtained with OTIS (OSU Tidal Inversion Software). The methods used to compute the model are described in detail by Egbert et al. (1994) and further by Egbert and Erofeeva (2002). The FES (Finite Element Solution) tide models, Lyard et al. (2006); Carrère et al. (2012), are based on the resolution of the tidal barotropic equations (T-UGO model) in a spectral configuration.

The ice concentration field used by the model is shown in Figure 2. The data are drawn from Walsh et al. (2015), monthly gridded sea ice concentration product based on observations from historical sources from 1850 onward. For each month we take a median value of the respective monthly ice concentrations from the period between January 1961 and December 1990. That is, every pane of Figure 2 represents a median of the 30 monthly values. The choosen period corresponds to the date range when majority of the observations were collected. We have used the median rather than mean or a single year concentration to reduce the effect of extreme years on the final field. The drawback of this approach is the possibility to increase the model errors in the areas where the ice-induced seasonal and decadal variations are significant.

ADCIRC was run in barotropic two-dimensional depth integrated (2DDI) mode using the fully consistent GWCE and momentum equation formulations. A quadratic friction law was used, with friction coefficient $C_{D_{bot}}$ set to 0.0025, following Dupont et al. (2002) and Dunphy et al. (2005). The model was run for 383 days, which included 17 days of spin up time.

2.5. Error metrics

To assess the quality of a tidal model an error metric has to be specified. Similarly to Dunphy et al. (2005) we use a single metric which combines both elevation and phase error and allows us to measure how well each constituent was modelled. At each station and for each constituent the error is defined as the magnitude of the observed constituent minus the modelled constituent evaluated in the complex plane

$$err = |H_0 e^{i\phi_0} - H_m e^{i\phi_m}| \tag{3}$$

where H_0, ϕ_0 are the observed amplitude and phase and H_m, ϕ_m are the modelled values. To evaluate the solutions for one constituent over broader areas, the root-mean-square (RMS) values over regions defined in Table 1 were calculated.

3. Model validation

Tidal amplitudes vary from a few centimeters in the west along the Arctic shelf to over 1m in the eastern areas of the Archipelago. Generally, the M2 component is the largest, with the exception of Boothia Bay where the K1 diurnal tide dominates, Figure 4.

The tidal motion in the Canadian Arctic Archipelago primarily originates from the tides in the Atlantic Ocean. The mainly semi-diurnal tidal signal enters the Hudson Strait at the eastern entrance with an amplitude about 3m and reaches its maximum in Leaf Basin. Further, the tidal wave propagates westward though the strait, around the coast of Hudson Bay in an anti-clockwise direction and forms two amphidromic points in the west-central and east-central parts of the bay and a degenerate one in James Bay.

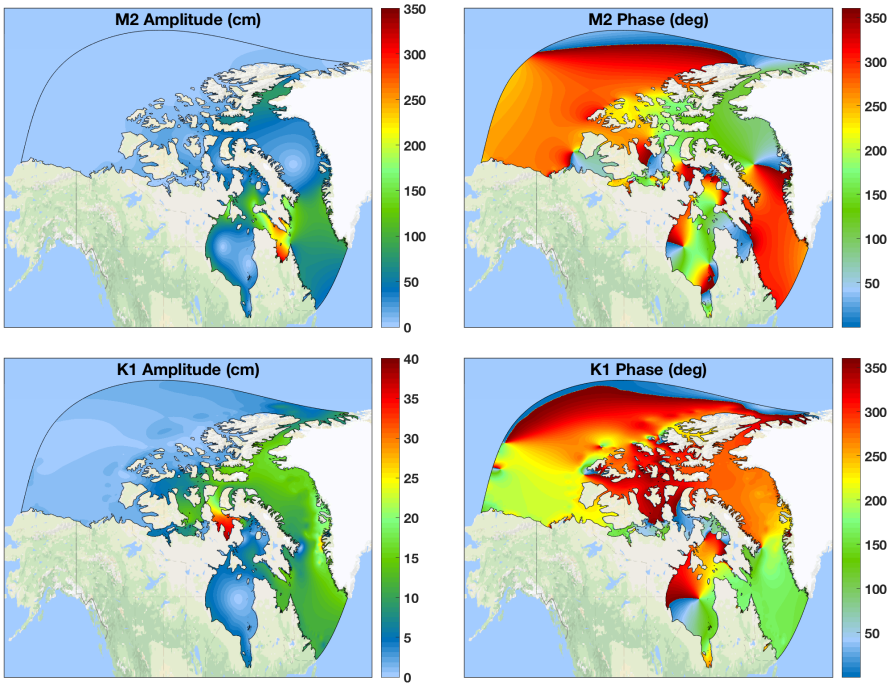

Figure 4: Annual mean amplitude and phase of the M2 and K1 tidal constituents.

The maximum M2 tidal amplitude of 1.25m occurs along the west coast of Hudson Bay.

A small portion of the tidal signal entering through the Labrador Sea flows into Baffin Bay forming an amphidromic system there. The semi-diurnal tidal wave propagates north along the west coast of Greenland, reaches the maximum amplitude of over 1m in Kane Basin and enters the Archipelago through Barrow Strait.

3.1. Comparison with the tide gauges

The RMS errors of the 8 major constituents evaluated over each region are shown in Figure 5. The prediction errors vary from region to region, reflecting the regional tidal range. However, in some cases the regional errors are dominated by larger errors at few locations. This is especially true for the K2, P1 and Q1 tidal constituents, due to partially missing data.

The largest regional errors for the semi-diurnal constituents are observed in Hudson Strait/Ungava Bay. It is worth noting that the tidal range in Ungava Bay competes with the Bay of Fundy for the title of the world's highest tides, O'Reilly et al. (2005). The obtained regional RMS error of 55cm is about 21% of the local tidal range and is, therfore, acceptable. Errors for the diurnal tide constituents are dominated by the errors in the Arctic South Central and Southeast regions. The semi-diurnal and diurnal tidal resonances in Ungava Bay and Boothia Bay respectively make these regions

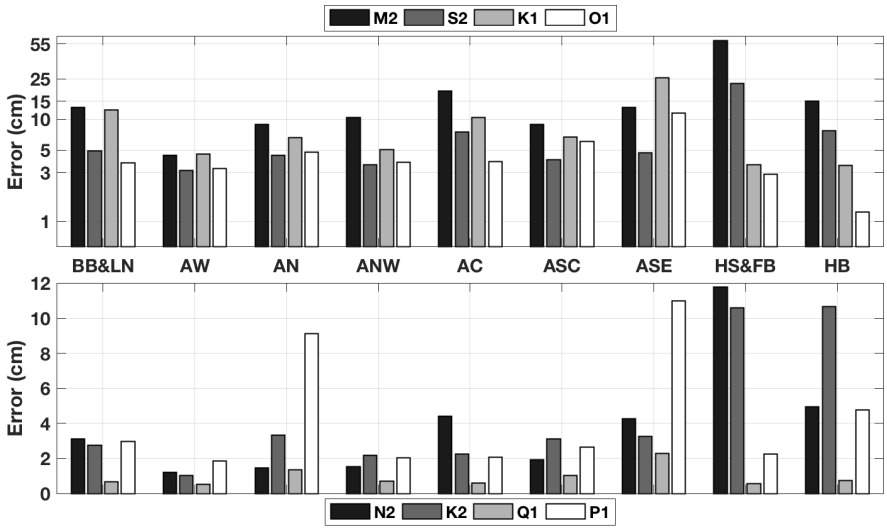

Figure 5: The regional RMS errors of the tidal constituents.

very sensitive to any inadequacy in bathymetric details and, therfore, difficult to model accurately. The maps of the computed tidal characteristics together with the amplitude and phase errors at the tide gauge stations are shown in Figures A.17-A.24.

In general, the model seems to under-predict tidal amplitudes more often than over-predict. Large amplitude errors for semi-diurnal constituents around Kane Basin suggest that the Nares Strait is not properly resolved. This can also contribute to the under-prediction of the tidal amplitudes on the eastern part of Devon Island. Large phase errors in the Arctic West region can indicate a problem with the open boundary forcing.

3.2. Tidal currents in the Central Region

The comparison of the observed and modelled tidal ellipse parameters for M2 and K1 is shown in Figure 6. As can be seen the modelled amplitude of the M2 major axis agrees quite well with the observations, with the exception of the currents at HM1, HM2 and HM3 which are under-predicted. The largest errors in the amplitude of the modelled K1 major axis are again observed at the JS2 and HM stations.

The model-data comparison for the tidal currents shows the same strange features as in Collins et al. (2011), such as good agreement at JS1 and poor at JS2, large differences in phases at various locations etc. In general, the modeled and observed currents show reasonable agreement when the observations cover most of the water column and are for long periods of time. That is, some of the model-data mismatch can be due to important seasonal changes in the tidal currents and important vertical structure in the tidal currents. Therefore, a three-dimensional model which accounts for vertical stratification and horizontal density gradients is required to address this issue.

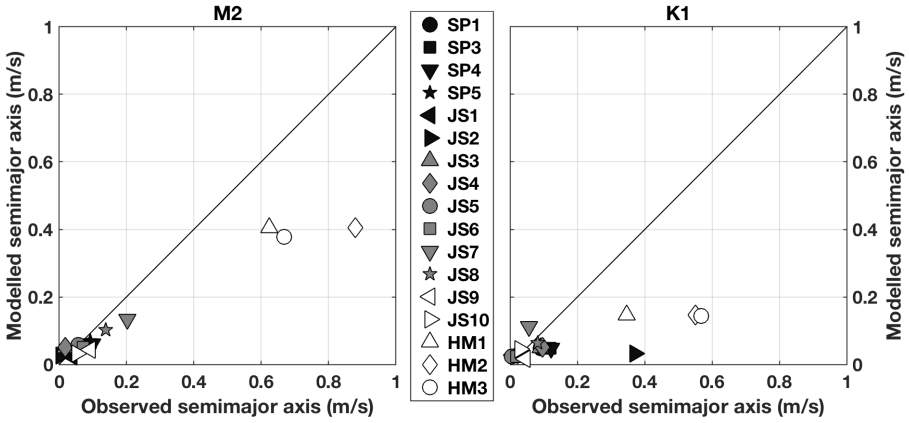

Figure 6: Comparison of the modelled and observed semi-major axis for the M2 (left) and K1 (right) currents.

4. Ice induced variability of tidal constants

4.1. Seasonal variations of the tidal constants

The ice induced variability of the tidal constituents are examined by partitioning the simulated yearly time series into slightly overlapping monthly segments and performing a harmonic analysis for each segment separately. Section Appendix B shows a detailed comparison of the modelled and observed seasonal cycle of the M2 amplitude at a number of tide gauges.

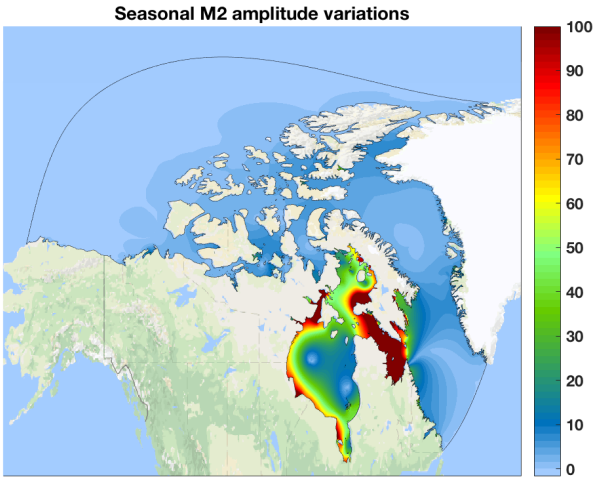

Figure 7: Seasonal (max- min) changes in the amplitude of M2 tidal constituent.

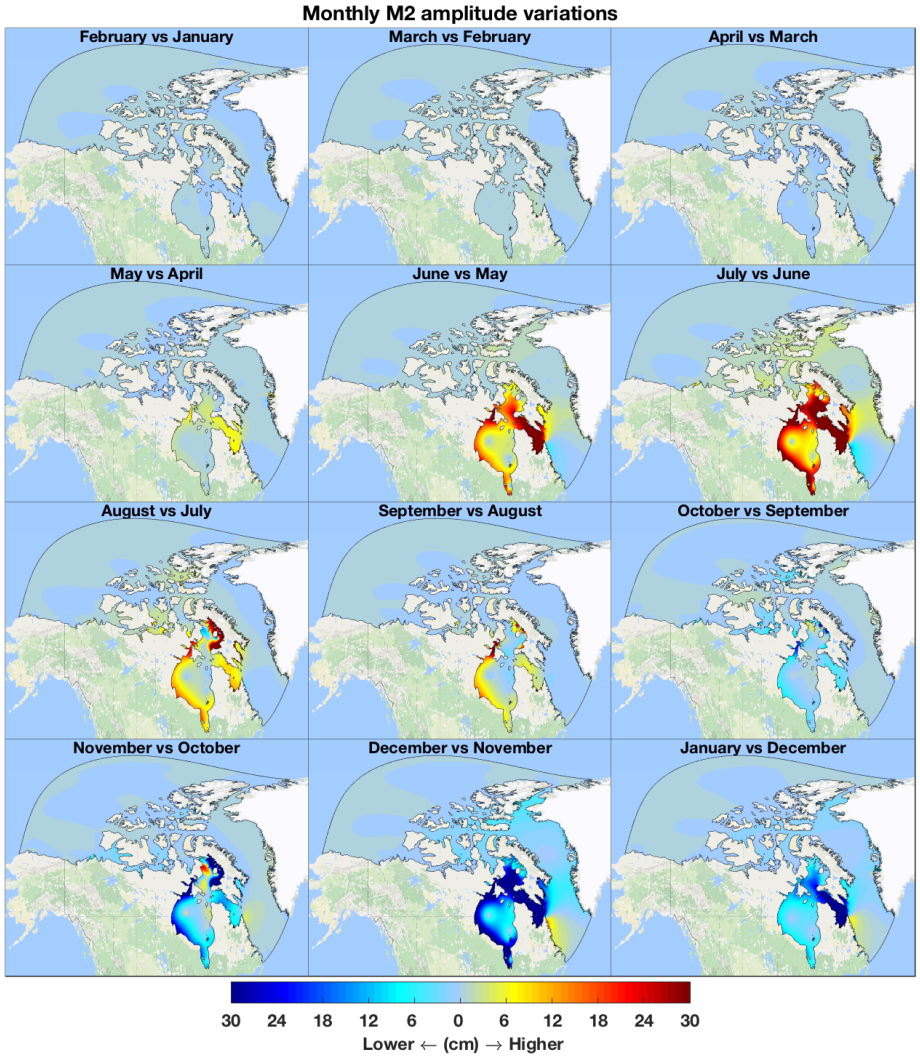

Figure 8: Monthly amplitude variations of M2 tidal constituent. Yellow/red colors indicate increase in amplitude with respect to the previous month.

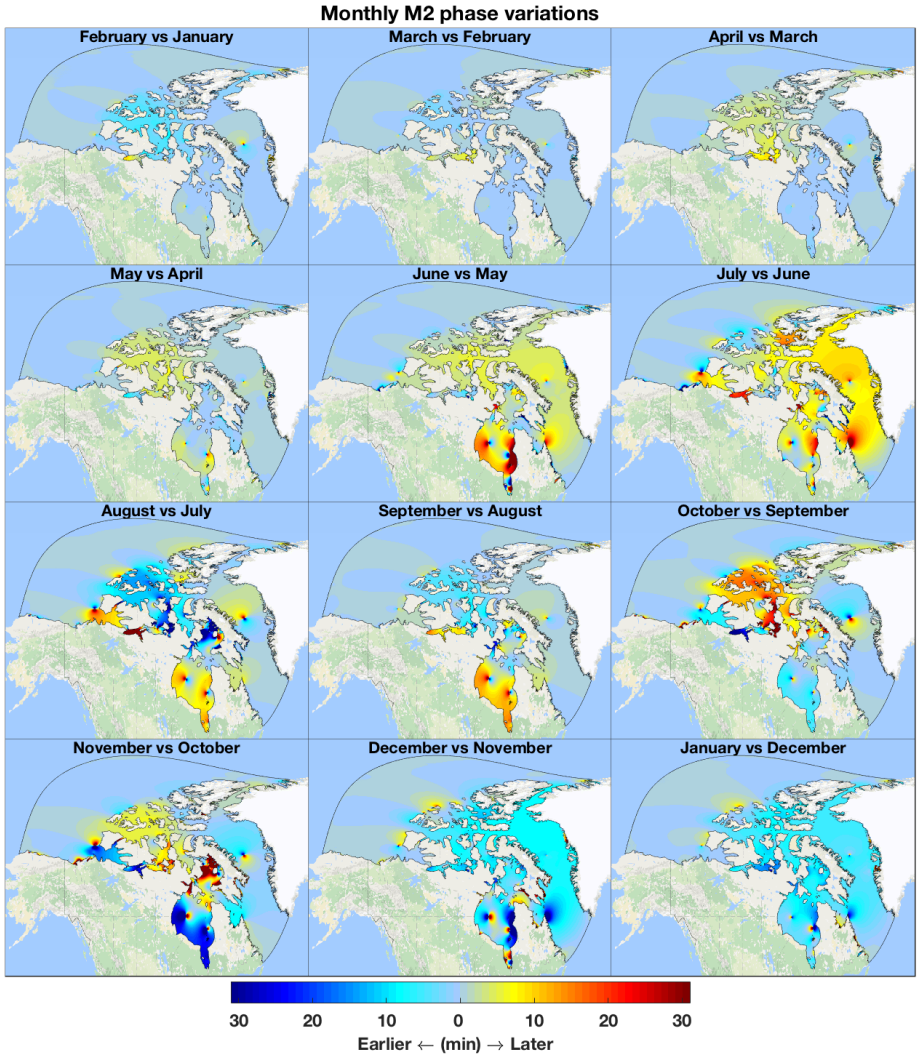

Figure 9: Monthly phase variations of M2 tidal constituent. Yellow/red colors indicate later arrival compared to the previous month.

Tidal motion in the entire model domain exibits a certain degree of variability. As can be seen from Figure 7 seasonal changes in the M2 amplitude (i.e. the difference between maximum and minimum) range between 5 and 10 cm in south Baffin Bay, Kane Basin, M'Clintock Channel, Lancaster Sound and Norwegian Bay. The amplitude variations reach about 50 cm along the west coast of Hudson Bay and James Bay, southwest of Foxe Basin. Summer to winter changes in M2 amplitude exceeding 1 m are observed in Roes Welcome Sound, Hudson Strait and Ungava Bay. As shown by Arbic et al. (2007) these regions are (nearly) resonant with the tidal forcing and, therefore, are very sensitive to the frictional effects of ice cover. In the Section 4.2 we will study the seasonality of the tidal dynamics in the Hudson Bay/Hudson Strait system in more details. Month to month changes in the amplitude of M2 tidal constituent are shown in Figure 8.

Month to month changes in the tidal phases (shown in Figure 9) are generally of order $10 - 20$ degrees. However, in some locations the differences up to 180 degrees are observed. These large phase variations are typically found in the vicinity of the amphidromic points and are due to their movement (see video in supplementary material). During the winter months the two amphidromic points in the west- and east-central parts of Hudson Bay move southward, resulting in the earlier arrival of the tide. This agrees with the theoretical considerations by Prinsenberg (1988). The amphidrome in the Baffin Bay moves westward and the one to the south-west of Banks Island moves towards the east.

4.2. Seasonality of tides in the HB/HS system from the analytical model by Cummins et al. (2010)

In this section we will use the simple analytical model by Cummins et al. (2010) to study seasonality of tides in the Hudson Bay/Hudson Strait system. Cummins et al. (2010) studied the semi-diunal responce in the Hudson Bay/Hudson Strait region by means of a simple model of a channel connected to an inner basin. Taking into account the mechanical impedance presented to the channel by Hudson Bay, they have shown that the fundamental channel mode has a natural period of oscillations close to that of the semi-diurnal tides.

The idealised model domain shown in Figure 10 consists of a basin of a surface area A_B connected to the ocean via a channel of uniform width W, length L and depth H. The channel is assumed to be sufficiently narrow so that rotational effects can be neglected. Assuming that water level and along-channel velocity have a simple harmonic form $(h, u) = (\bar{h}(x), \bar{u}(x))e^{i\omega t}$, the linearized continuity equations can be combined with the along-strait momentum equation to form the second order boundary value problem for the complex water level amplitude

$$\frac{d^2\bar{h}}{dx^2} + k^2\bar{h} = 0 \tag{4}$$

Here $k^2 = k_0^2(1 - i\delta)$ is the complex wavenumber, with $k_0^2 = \omega^2/gH$, the linear drag coefficient r and the non-dimensional channel friction parameter $\delta = r/\omega$. The boundary condition for Equation (4) at the channel entrance ($x = 0$) is

$$\bar{h}(0) = h_0, \tag{5}$$

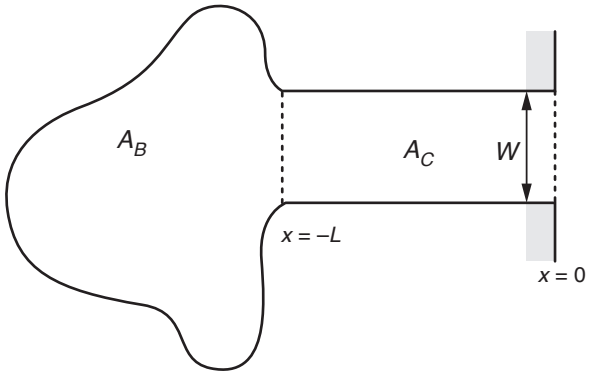

Figure 10: The idealized model domain of a basin connected to the ocean via a channel of uniform width. Adapted from Cummins et al. (2010).

where h_0 is the amplitude of the sea level displacement associated with a prescribed incoming wave. At the channel-basin junction ($x = -L$) conservation of mass is required. Assuming that the amplitude of sea surface displacement averaged over the basin can be written in terms of the channel elevation at the basin junction as $\bar{h_B} = \alpha\bar{h}(-L)$, this gives

$$\frac{d\bar{h}}{dx} = -\frac{\alpha}{\gamma}k^2 L\bar{h}, \tag{6}$$

with $\gamma = A_C/A_B$. The generally complex constant α represents basin impedance and is a function of frequency that depends on the size and geometry of the basin. An appropriate value for α can be determined using results from the numerical tidal model.

Solution of Equation (4) subject to the boundary conditions (5) and (6) is derived by Cummins et al. (2010) and is given by

$$\bar{h}(x) = h_0\left[\cos kx - \frac{\sin kL + \frac{\alpha kL}{\gamma}\cos kL}{\cos kL - \frac{\alpha kL}{\gamma}\sin kL}\sin kx\right] \tag{7}$$

The water level elevation is then expressed in terms of an amplitude and phase as $h(x,t) = |\bar{h}(x)|\cos(\omega t - \phi(x))$ with $\phi(x) = -\operatorname{atan2}(Im[\bar{h}(x)], Re[\bar{h}(x)])$.

The channel response to the tidal forcing given by Equation (7) is governed by the amplitude of the forcing h_0 and three non-dimensional parameters α/γ, δ and $k_0 L$ depending on the forcing frequency, the bottom drag coefficient and dimensions of the basin and channel. The parameter γ representing ratio of the basin to channel area is set to 0.15. Similary to Cummins et al. (2010) we make an empirical estimate of α using results from the numerical model forced at the M2 frequency. Since the basin impedance is related to the dissipation of energy it could vary seasonally due to the additional friction associated with the ice cover. We, therefore, estimated α_{summer} and α_{winter} from two model runs representing summer and winter conditions. The value of $C_{D_{ice}}$ was set to $2.5 * 10^{-3}$. Variation over an M2 tidal cycle of the modelled surface elevation averaged over the Hudson Bay-Foxe Basin and along its junction with

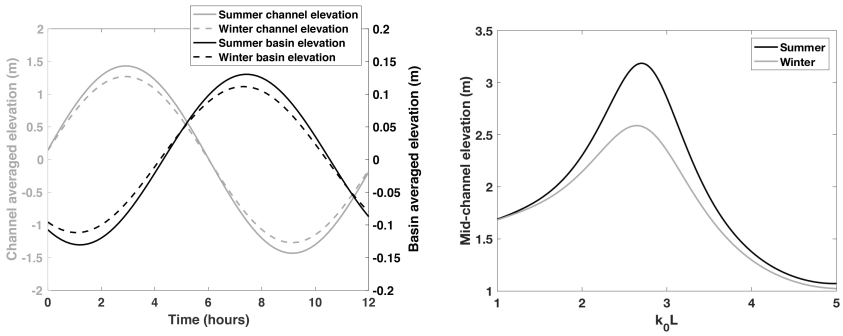

(a) (b)

Figure 11: (a) Surface elevation averaged over Hudson Bay-Foxe Basin (right scale), and along the entrance to Hudson Strait (left scale) obtained from the numerical model for the summer and winter seasons. (b) Analytical model response at mid-channel as a function of $k_0 L$ for the summer and winter seasons.

Hudson Strait is shown in Figure 11(a). These are related by the complex constants $(|\alpha|, arg(\alpha))_{summer} = (0.091, -130°)$ and $(|\alpha|, arg(\alpha))_{winter} = (0.088, -127°)$ for the summer and winter seasons respectively.

During the summer season the Hudson Strait/Hudson Bay area is mostly ice-free, whereas during the winter season it is characterized by nearly 100% ice coverage. The linear friction coefficient $r \approx C_D U/H$ was, therefore, calculated based on $C_D = C_{D_{bot}} = 2.5 * 10^{-3}$ for the summer season and on $C_D = C_{D_{bot}} + C_{D_{ice}} = 5 * 10^{-3}$ for the winter, using a tidal speed of $U \approx 1m/s$, and the average channel depth H of 235m. For the semi-diurnal frequency $\omega \approx 1.4 * 10^{-4}$ these give $\delta = 0.076$ and 0.152 for summer and winter respectively. Inspecting the dependency of the sea level elevation at the middle of the channel on the value of $k_0 L$, shown in Figure 11(b) gave the value of 2.7 at resonance. The amplitude of the forcing at the mouth of the channel was set to 1.5m.

Figure 12 shows the amplitude of along channel dispacement given by Equation (7) with the parameters as defined above for the summer and winter seasons. The analytical model predicts the maximum amplitude of 3.2m in the summer (2.6m in the winter) to be found at $x/L \approx -0.55$. At the basin-channel junction the amplitude is predicted to reduce from approximately 1.7m in the summer to 1.4m in the winter. These values agree reasonably well with the results of the numerical model, 3.05m in the summer (2.55m in the winter) at the midchannel and 1.66m (1.49m) at the basin-channel junction.

Using a Taylor solution of a reflecting Kelvin wave in a rectangular basin Prinsenberg (1988) has demonstrated that the ice cover causes nearly the same amount of damping for the tides as that used to represent bottom friction. The additional friction due to the ice cover causes about 10% M2 amplitude decrease at the Churchill station, assuming that the amplitude at the basin entrance does not change. If, as results above suggest, amplitude of the M2 tide entering the Hudson Bay is reduced by $\sim$ 19% during winter, then the amplitude at Churchill should decrease by approximately 27%. As can be seen from Figure 26(f) (dotted line), the modelled amplitude reduces by 25% in January (100% ice coverage) compared to September (ice-free period). Thus, the

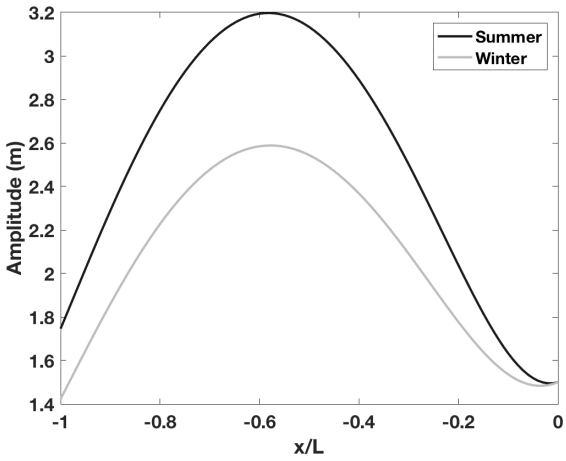

Figure 12: Amplitude of the along channel displacement.

amplitude reduction shown by the numerical model agrees very well with the simple analytical model of the channel resonance and reflected Kelvin wave.

Moreover, Arbic et al. (2009); Arbic and Garrett (2010) have shown that the open ocean tide can be affected (generally reduced) by the presence of a resonant shelf. The 'back-effect' is especially large if the open ocean itself is close to resonance and the shelf friction is small. Therefore, an increase of shelf friction due to presence of ice cover should lead to an increase in ocean tides in the northern Labrador Sea. Increased amplitudes of the M2 tidal constituent during winter months observed at Nain and Qaqortoq stations (see Figure 26(g) and 26(h)) support these conjecture.

Thus, the discrepancy with the observed seasonal variations in the western Hudson Bay may be due to the forcing on the eastern entrance of the Hudson Strait, which was kept constant by the domain's open boundary conditions. Therefore, the range of seasonal variations of the tidal constants at the model domain open boundary and its influence on the tidal dynamics in the area needs to be further investigated. This will be done in a separate paper.

4.3. Decadal scale variations of the ice induced tidal seasonality

Evidence of the climate change comes, among others, from the decrease in extent and thickness of the Arctic sea ice, Stroeve et al. (2007); Comiso et al. (2008); Rothrock et al. (1999). These changes could significantly impact the tidal dynamics in the Canadian Arctic Archipelago. In this section we explore how the ice induced tidal seasonality has changed in the course of the past six decades.

We used the model setup as described in Section 2.4 with two different ice concentration fields, shown in Figures C.27-C.28. The fields are drawn from Walsh et al. (2015) and correspond to the periods from 1958 to 1962 and from 2008 to 2012. Figure 13 depicts the difference in the monthly ice concentration between the periods. During the winter months the area remains fully ice covered, with the exception of

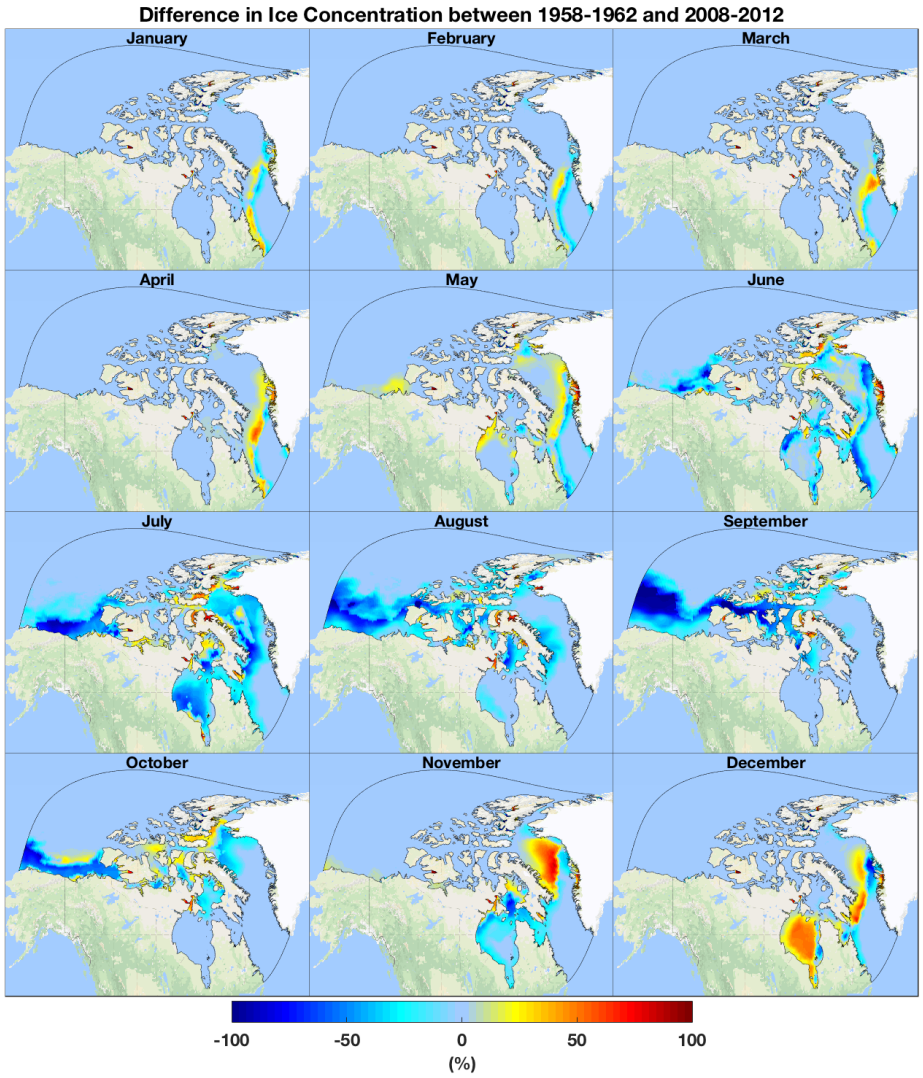

Figure 13: Difference in the monthly ice concentration between the periods of 1958-1962 and 2008-2012. Yellow/red colors indicate higher concentration in 2008-2012 compared to 1958-1962.

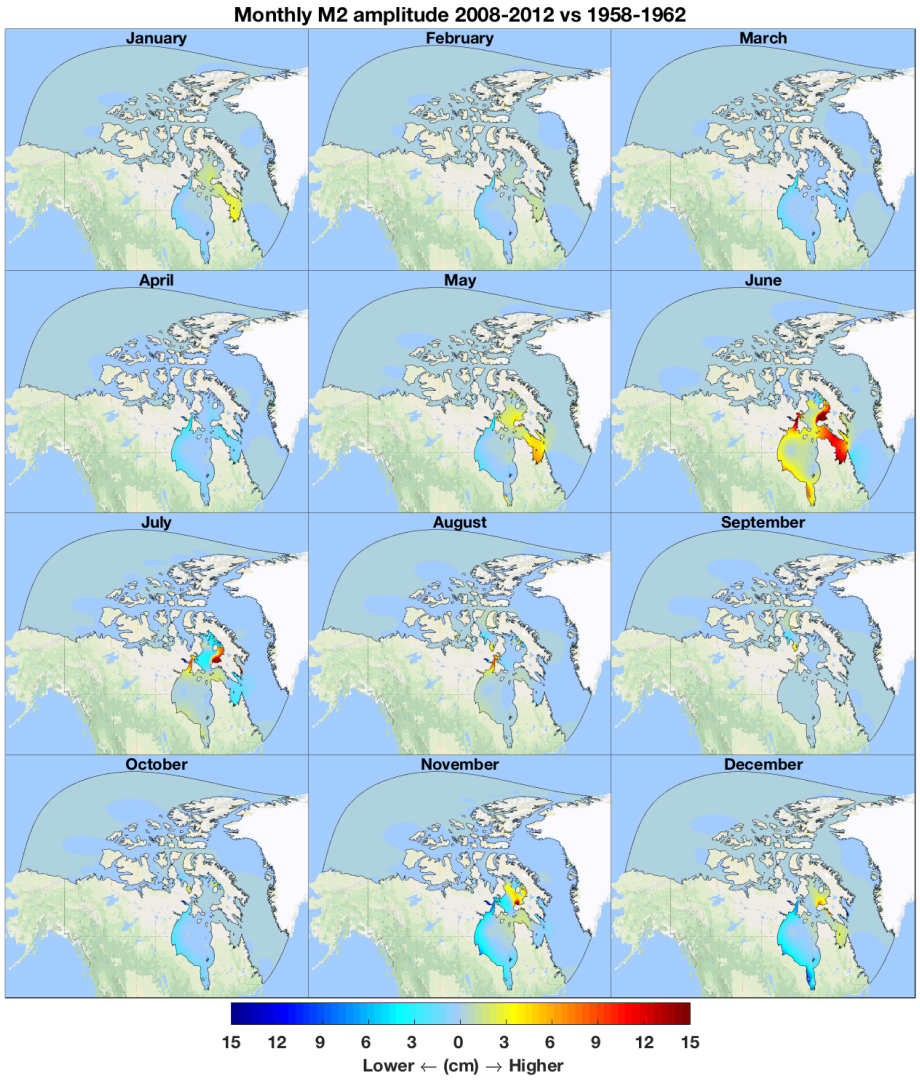

Figure 14: Difference in the monthly M2 amplitude between the periods of 1958-1962 and 2008-2012. Yellow/red colors indicate higher amplitude in 2008-2012 compared to 1958-1962.

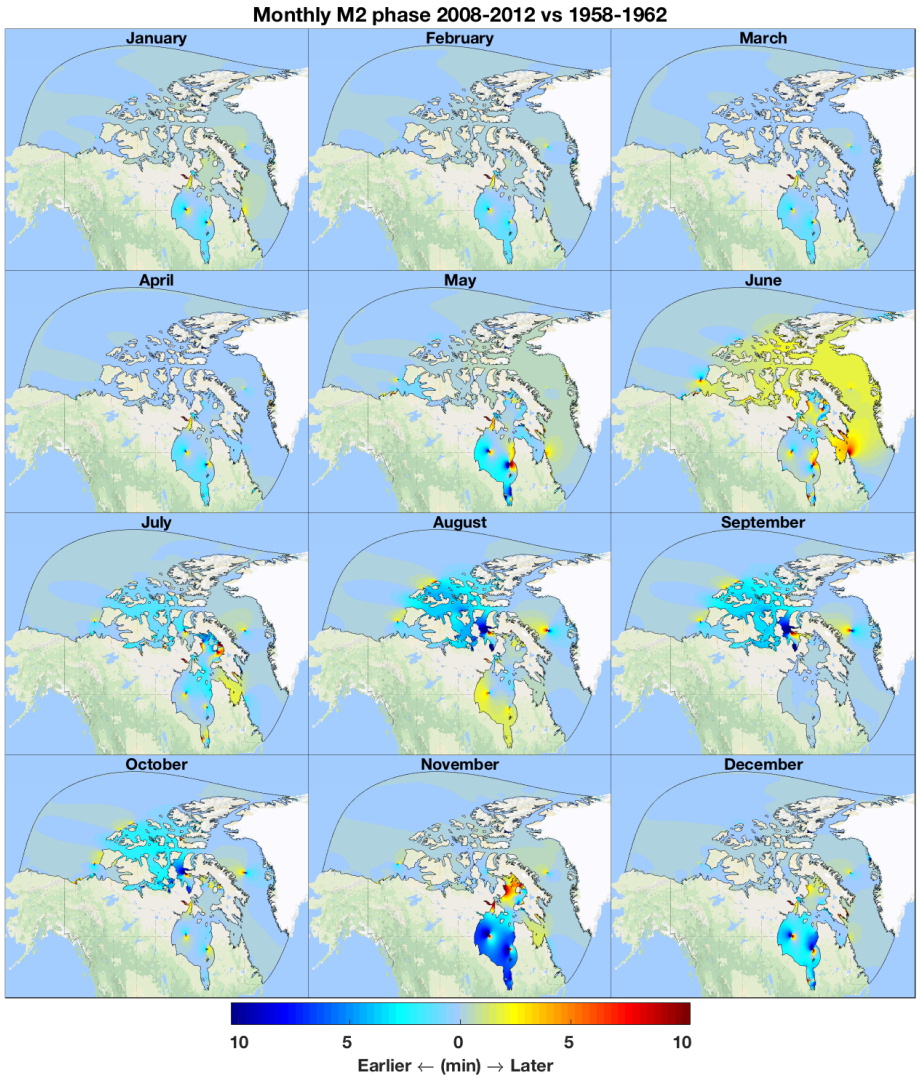

Figure 15: Difference in the monthly M2 phase between the periods of 1958-1962 and 2008-2012. Yellow/red colors indicate later arrival in 2008-2012 compared to 1958-1962.

the Northern Labrador Sea which remains ice-free thoughout the year. The extent of the winter ice changed only slightly between the lustrums. The ice started to melt approximately a month earlier and the extent of summer ice decreased significantly in the 2008-2012 period compared to the period of 1958-1962. Although the areas which were ice-free during the summer started to freeze later in the 2008-2012 period, the ice cover formed faster. As a result, December ice concentrations in these areas were higher during the 2008-2012 period. Please note that the decadal scale results are sensitive to the quality of the early observations. As described in Walsh et al. (2015) the data for the earlier period depends on ship logs and naval records.

The resulting monthly M2 amplitudes and phases for both periods are shown in Figures C.29-C.32. Changes in the monthly amplitudes, shown in Figure 14, reflect closely the changes in the monthly ice concentrations, lower ice concentrations result in higher amplitudes and vise versa. The largest amplitude differences are predicted in the Hudson Strait/Hudson Bay area. As we have shown earlier, the area is very sensitive to friction due to its closeness to resonance with the semi-diurnal tidal frequencies. The amplitude increase of $12cm$ is predicted in June of 2008-2012 comparing to June of 1958-1962 correspond to the earlier melting of ice during that period. Faster freezing during the 2008-2012 period resulted in approximately $5cm$ lower amplitudes along the western coast of Hudson Bay in November and December.

Changes in the monthly M2 phases are shown in Figure 15. Yellow/red colors indicate that the tide arrived later in the 2008-2012 period than in 1958-1962. The relation between the ice concentrations and the phase of the tide is more complicated. Decreased ice concentrations could lead to later as well as earlier arrival of tide depending on the wave form of the tide in a specific area. If the tide propagates more or less along a straight coast, then decrease in the ice friction will lead to an increase of the phase velocity, Prinsenberg (1988). The increased phase velocity causes an advancement of the arrival time, as predicted in the Arctic West, Northwest, Central and South Central regions from July to August of 2008-2012 (see Figure 3 and Table 1 for the definition of the regions). In Hudson Bay the earlier melting and reduced July-August ice friction causes the amphidromic points to be located more northward compared to the 1958-1962 period. This causes delay in arrival of the tide along the Hudson Bay west coast during the summer of 2008-2012. The opposite is predicted in November and December due to the faster freezing.

5. Tidal mixing

Tides have long been recongnized to be an important mixing mechanism in shallow seas. Positions of tidal mixing fronts are commonly identified using a stratification parameter originally developed by Simpson and Hunter (1974) for thermally stratified seas. However, as shown by Bowman and Esaias (1981), it can be considered a general parameter relating a constant buoyancy input to tidal mixing energy irregardless of the nature of the input. Therefore, despite the fact that fresh water addition via ice melting or river run off has large effect on the density structure in the Canadian Arctic Archipelago, the parameter can also be used to identify tidal mixing front positions here (Drinkwater and Jones (1987); Rudels et al. (1991)).

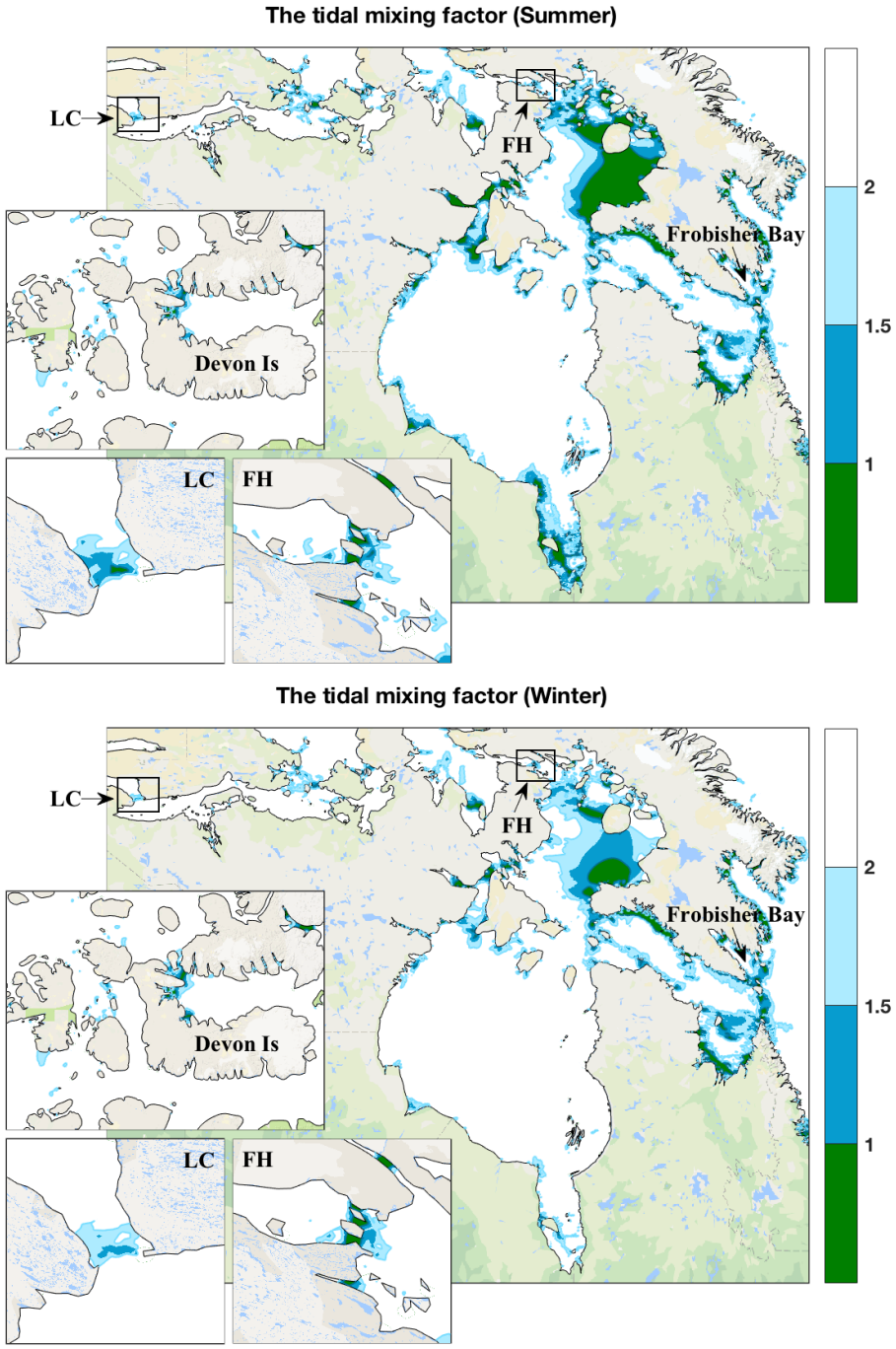

Figure 16: The RMS summer (top) and winter (bottom) tidal mixing parameter. The insets show regions around Devon Island including Hell Gate, Cardigan Channel, Penny Strait and Queens Channel (top), Lambert Channel (bottom left) and the Fury and Hecla strait (bottom right).

Here we calculated distribution of the tidal mixing parameter as defined by Pingree and Griffiths (1978), $\lambda = \log_{10}(h/C_D|u_s|^3)$, where h denotes the water depth, C_D is the bottom drag coefficient and u_s is the depth averaged tidal stream velocity amplitude. The root-mean-square (RMS) of tidal currents were reconstructed from the eight tidal constituents as given by the model for the winter (January to March) and summer (August to October) periods. The drag coefficient C_D was calculated according to Equation (1) using the ice concentration field shown in Figure 2.

Although, the tidal currents vary significantly throughout the year, the larger part of the domain has values of λ greater than 2 for both winter and summer periods indicating a stratified water column. The well-mixed areas ($\lambda < 1$) are found in the southeast of Foxe Basin, along the southwest coast of Hudson Bay and James Bay, Ungava Bay and in several areas with narrow channels or shallow sills shown in Figure 16. These are the areas with strong tidal currents and tidal energy dissipation.

The upward heat transfer which occurs through vertical mixing of warmer deep water towards the surface can enhance melting of the ice cover or even prevent ice from forming (Smith et al. (1990)). Therefore, as shown by Hannah et al. (2008), the parameter λ can be used to identify areas where tidal mixing can contribute to the formation and maintenance of the sensible heat polynyas. For both the maximum (summer) and minimum (winter) stream velocity magnitude, the tidal mixing parameter λ is found to be less than 2 in many areas where recurring polynyas are known to form, see for example Barber and Massom (2007). Our study indicate that, besides the ones shown in Hannah et al. (2008), a polynya in Roes Welcome Sound, Akimiski Strait, Frobisher Bay and two polynyas in Foxe Basin could be of tidal nature.

6. Discussion

Tidal models have undergone a dramatic improvement since the first Topex/Poseidon satellite altimeter mission was launched. The open ocean barotropic tides in the latitude band coverd by the altimeters are now known with about 98% accuracy (0.5-0.7 cm error compared to a signal of 30 cm). Although our knowlege of shelf and coastal tides has also advanced in the recent years, the relative errors here are still much higher (up to 16% according to Stammer et al. (2014)) than for open ocean barotropic tides. Significant efforts are required to develop an accurate tidal model of each specific shelf/coastal region. This is especially true for the high-latitude areas such as Canadian Arctic Archipelago considered here. Besides issues common to the majority of shelf regions, such as uncertainties in bathymetric data and sparse observations, the presence of seasonally varying ice cover poses additional difficulties.

Here, a tidal prediction system for the Canadian Arctic Archipelago has been completed for the eight major constituents (M2, N2, S2, K2, K1, O1, P1 and Q1) using ADCIRC. Boundary conditions are a combination of FES2004/2012 and TPXO8 global solutions. The RMS error of the tidal constituents averaged over the entire model domain is about 21cm for M2 and (8, 5, 6, 5, 11, 1 and 5) cm for (S2, N2, K2, O1, K1, Q1 and P1), respectively. The errors for the semi-diurnal constituents are dominated by the errors in the Hudson Strait/Ungava Bay system. The poorly known bathymetry is an important factor which limits accuracy of the tidal modeling in this resonant area.

In order to study the ice induced variability of the tidal constants, the simulated water level time series were partitioned into monthly segments and analysed separately. The analysis shows that the tidal dynamics of the entire model domain are subject to seasonal variations. Larger phase differences are often observed in the vicinity of the amphidromic points and are caused by their relocation. The larger amplitude differences are observed in the resonant basins. These are also the areas where the seasonal variations have changed significantly in the past six decades. More specifically, earlier melting of ice in the Hudson Bay/Hudson Strait area during the last decade resulted in up to $12cm$ amplitude increase in June compared to early 60s. Note also, that large RMS error of the M2 tidal constituent in the region can be partially attributed to this change.

Discrepancy between the observed and modelled seasonal variability of the tidal constants in the Hudson Bay system could be due to the open boundary conditions which were assumed to be independent of the coastal dynamics. It was shown by Arbic et al. (2009) and Arbic and Garrett (2010) that continental shelfs can significantly impact tides in the deep ocean, especially if the shelf region is close to resonance with tidal forcing. As shown by Webb (2014), tidal dynamics in the Hudson Bay system are dominated by four nearly overlaping tidal resonances. These resonances acting together make the region around Hudson Bay (including the Labrador Sea, Baffin Bay, and Canadian Arctic straits) the most important area for tidal energy dissipation, Egbert and Ray (2001). Chevalier et al. (2013) has demonstrated using the FES2012 hydrodynamic solution that the tidal dissipation in Hudson Bay is crutial for the accuracy of global tidal solutions especially in the Atlantic. Varying ice cover seasonally changes tidal dissipation in the Hudson Bay area and, therefore, not only modifies tidal characteristics locally, but also impacts tides in the remote areas. Tidal seasonality in the Subarctic ocean is also evident from the satellite altimeter data. Figure 1 from Fok et al. (2013) clearly shows that SSH anomaly residual during the winter season is 15 – 30% larger than that during the summer season. This also means that the accuracy of the global tidal solutions can vary significantly between the seansons. Therefore, the ice induced seasonal and decadal variations of barotropic tides remains an outstanding subject for further research.

7. Acknowledgments

The authors would like to thank David Greenberg and Florent Lyard for their detailed comments on an early stage of this paper. We are immensely grateful to van Scheltinga Arjen Terwisscha van Scheltinga for his help with generation of the grid. We would also like to show our gratitude to Joannes Westerink and the Computational Hydraulics Laboratory (CHL) at the University of Notre Dame for the help with learning ADCIRC and setting up the numerical model.

Computing time on a national supercomputer system used for this work is financed by the Netherlands Organisation for Scientific Research (NWO).

NWO
Netherlands Organisation for Scientific Research

8. Bibliography

Arbic, B. K., Garrett, C., 2010. A coupled oscillator model of shelf and ocean tides. Continental Shelf Research 30 (6), 564 – 574.

Arbic, B. K., Karsten, R. H., Garrett, C., 2009. On tidal resonance in the global ocean and the backeffect of coastal tides upon openocean tides. Atmosphere-Ocean 47 (4), 239–266.

Arbic, B. K., St-Laurent, P., Sutherland, G., Garrett, C., 2007. On the resonance and influence of the tides in Ungava Bay and Hudson Strait. Geophysical Research Letters 34 (17).

Barber, D., Massom, R., 2007. Chapter 1: The role of sea ice in arctic and antarctic polynyas. Polynyas: Windows to the World 74, 1 – 54.

Bowman, M. J., Esaias, W. E., 1981. Fronts, stratification, and mixing in long island and block island sounds. Journal of Geophysical Research: Oceans 86 (C5), 4260–4264.

Carrère, L., Lyard, F., Cancet, M., Guillot, A., Roblou, L., 2012. Fes2012: A new global tidal model taking advantage of nearly 20 years of altimetry. Proceedings of meeting "20 Years of Altimerty".

Chen, C., Gao, G., Qi, J., Proshutinsky, A., Beardsley, R. C., Kowalik, Z., Lin, H., Cowles, G., 2009. A new high-resolution unstructured grid finite volume arctic ocean model (ao-fvcom): An application for tidal studies. Journal of Geophysical Research: Oceans 114 (C8), c08017.

Cheng, Y., Andersen, O. B., 2011. Multimission empirical ocean tide modeling for shallow waters and polar seas. Journal of Geophysical Research: Oceans 116 (C11).

Chevalier, L., Lyard, F., Greenberg, D., Soufflet, Y., Apr. 2013. Tidal hydrodynamics of the Hudson Bay and its impact in the global ocean tide. In: EGU General Assembly Conference Abstracts. Vol. 15 of EGU General Assembly Conference Abstracts. pp. EGU2013–1132.

Codiga, D. L., 2011. Unified Tidal Analysis and Prediction Using the UTide Matlab Functions. Graduate School of Oceanography, University of Rhode Island.

Collins, A. K., Hannah, C. G., Greenberg, D., 2011. Validation of a High Resolution Modelling System for Tides in the Canadian Arctic Archipelago. Canadian Technical Report of Hydrography and Ocean Sciences 273:vii+72pp.

Comiso, J. C., Parkinson, C. L., Gersten, R., Stock, L., 2008. Accelerated decline in the arctic sea ice cover. Geophysical Research Letters 35 (1), l01703.

Cummins, P. F., Karsten, R. H., Arbic, B. K., 2010. The semidiurnal tide in Hudson strait as a resonant channel oscillation. Atmosphere-Ocean 48 (3), 163–176.

Dietrich, J., Tanaka, S., Westerink, J., Dawson, C., Luettich, R., Zijlema, M., Holthuijsen, L., Smith, J., Westerink, L., Westerink, H., 2012. Performance of the unstructured-mesh, SWAN+ADCIRC model in computing hurricane waves and surge. J. Sci. Comput. 52, 468–497.

Drinkwater, K., Jones, E., 1987. Density stratification, nutrient and chlorophyll distributions in the Hudson Strait region during summer and their relation to tidal mixing. Continental Shelf Research 7 (6), 599 – 607.

Dunphy, M., Dupont, F., Hannah, C., Greenberg, D., 2005. Valdiation of a modelling system for tides in the Canadian Arctic Archipelago. Canadian Technical Report of Hydrography and Ocean Sciences 243:vi+70pp.

Dupont, F., Hannah, C., Greenberg, D., Cherniawsky, J., Naimie, C., 2002. Modelling system for tides for the Northwest Atlantic Coastal Ocean. Canadian Technical Report of Hydrography and Ocean Sciences 221, vii + 72pp.

Egbert, G. D., Bennett, A. F., Foreman, M. G. G., 1994. TOPEX/POSEIDON tides estimated using a global inverse model. Journal of Geophysical Research: Oceans 99 (C12), 24821–24852.

Egbert, G. D., Erofeeva, S. Y., 2002. Efficient Inverse Modeling of Barotropic Ocean Tides. Journal of Atmospheric and Oceanic Technology 19, 183–204.

Egbert, G. D., Ray, R. D., 2001. Estimates of m2 tidal energy dissipation from topex/poseidon altimeter data. Journal of Geophysical Research: Oceans 106 (C10), 22475–22502.

Farvandsvæsenet, 2000. Tidevandstabeller 2001 for grønlandske farvande.

Fok, H. S., Shum, C. K., Yi, Y.-C., Braun, A., Iz, H. B., Aug 2013. Evidences of seasonal variation in altimetry derived ocean tides in the subarctic ocean. Terrestrial, Atmospheric and Oceanic Sciences 24 (4I), 605–613.

Furevik, T., Foldvik, A., 1996. Stability at m2 critical latitude in the barents sea. Journal of Geophysical Research: Oceans 101 (C4), 8823–8837.

Geuzaine, C., Remacle, J.-F., 2009. Gmsh: A 3-D finite element mesh generator with built-in pre- and post-processing facilities. International Journal for Numerical Methods in Engineering 79 (11).

Godin, G., Barber, F., 1980. Variability of the tide at some sites in the canadian arctic. Arctic 33(1), 30–37.

Hannah, C., Dupont, F., Collins, A., Dunphy, M., Greenberg, D., 2008. Revisions to a Modelling System for Tides in the Canadian Arctic Archipelago. Canadian Technical Report of Hydrography and Ocean Sciences 259:vi+62pp.

Henry, R., Foreman, M., 1977. Numerical model studies of semidiurnal tides in the southern beaufort sea. Pacific Marian Science Report, No. 7711. Victoria: Inst. Ocean Sciences 71.

Jakobsson, M., Mayer, L. A., Coakley, B., Dowdeswell, J. A., Forbes, S., Fridman, B., Hodnesdal, H., Noormets, R., Pedersen, R., Rebesco, M., Schenke, H. W., Zarayskaya, Y., Accettella, D., Armstrong, A., Anderson, R. M., Bienhoff, P., Camerlenghi, A., Church, I., Edwards, M., Gardner, J. V., Hall, J. K., Hell, B., Hestvik, O. B., Kristoffersen, Y., Marcussen, C., Mohammad, R., Mosher, D., Nghiem, S. V., Pedrosa, M. T., Travaglini, P. G., Weatherall, P., 2012. The international bathymetric chart of the arctic ocean (IBCAO) version 3.0. Geophysical Research Letters.

Joyce, T. M., Proshutinsky, A., 2007. Greenland's Island Rule and the Arctic Ocean circulation. Journal of Marine Research 65 (5), 639–653.

Kagan, B., Sofina, E., 2010. Ice-induced seasonal variability of tidal constants in the arctic ocean. Continental Shelf Research 30 (6), 643 – 647, tides in Marginal Seas - A special issue in memory of Prof Alexei Nekrasov.

Kagan, B. A., Romanenkov, D. A., 2007. On the variability of tidal constants induced by the influence of one subsystem on another. Izvestiya, Atmospheric and Oceanic Physics 43 (3), 357–362.

Kagan, B. A., Romanenkov, D. A., Sofina, E. V., 2007. Modeling the tidal ice drift and ice-induced changes in tidal dynamics on the siberian continental shelf. Izvestiya, Atmospheric and Oceanic Physics 43 (6), 766–784.

Kowalik, Z., 1981. A Study of the M-2 Tide in the Ice-Covered Arctic Ocean. Modeling, Identification and Control 2 (4), 201–223.

Langleben, M. P., 1982. Water drag coefficient of first-year sea ice. Journal of Geophysical Research: Oceans 87 (C1), 573–578.

Luettich, R., Westerink, J., 2004. Formulation and numerical implementation of the 2D/3D ADCIRC Finite Element Model Version 44.XX.

Lyard, F., Lefevre, F., Letellier, T., Francis, O., 2006. Modelling the global ocean tides: modern insights from FES2004. Ocean Dynamics 56 (5), 394–415.

Macklin, S. A., 1983. Wind drag coefficient over first-year sea ice in the Bering Sea. Journal of Geophysical Research: Oceans 88 (C5), 2845–2852.

Madsen, O., Bruno, M., 1987. A methodology for the determination of drag coefficients for ice floes. Journal of Offshore Mechanics and Arctic Engineering 109 (4), 381–387.

Makinson, K., Holland, P., Jenkins, A., Nicholls, K., Holland, D., 2011. Influence of tides on melting and freezing beneath filchner-ronne ice shelf, antarctica. Geophysical Research Letters 38 (6).

Müller, M., Cherniawsky, J. Y., Foreman, M. G. G., von Storch, J.-S., 2014. Seasonal variation of the m2 tide. Ocean Dynamics 64 (2), 159–177.

Murty, T. S., 1985. Modification of hydrographic characteristics, tides, and normial modes by ice cover. Marine Geodesy 9 (4), 451–468.

Murty, T. S., Polavarapu, R. J., 1979. Influence of an ice layer on the propagation of long waves. Marine Geodesy 2 (2), 99–125.

O'Reilly, C. T., Solvason, R., Solomon, C., 2005. Where are the world's largest tides? in BIO Annual Report 2004 in Review, edited by J. Ryan, pp. 4446, Biotechnol. Ind. Org., Washington, D. C.

Pease, C. H., Salo, S. A., Overland, J. E., 1983. Drag measurements for first-year sea ice over a shallow sea. Journal of Geophysical Research: Oceans 88 (C5), 2853–2862.

Pingree, R. D., Griffiths, D. K., 1978. Tidal Fronts on the Shelf Seas Around the British Isles. J. Geophys. Res. 83, 4615–4622.

Prinsenberg, S. J., 1988. Damping and Phase Advance of the Tide in Western Hudson Bay by the Annual Ice Cover. Journal of Physical Oceanography 18 (11), 1744–1751.

Robertson, R., 2013. Tidally induced increases in melting of amundsen sea ice shelves. Journal of Geophysical Research: Oceans 118 (6), 3138–3145.

Rothrock, D. A., Yu, Y., Maykut, G. A., 1999. Thinning of the arctic sea-ice cover. Geophysical Research Letters 26 (23), 3469–3472.

Rudels, B., Larsson, A.-M., Sehlstedt, P.-I., 1991. Stratification and water mass formation in the arctic ocean: some implications for the nutrient distribution. Polar Research 10 (1), 19–32.

Saucier, F. J., Senneville, S., Prinsenberg, S., Roy, F., Smith, G., Gachon, P., Caya, D., Laprise, R., 2004. Modelling the sea ice-ocean seasonal cycle in Hudson Bay, Foxe Basin and Hudson Strait, Canada. Climate Dynamics 23 (3), 303–326.

Simpson, J., Hunter, J. R., 1974. Fronts in the Irish Sea. Nature 250, 404–406.

Smith, S. D., Muench, R. D., Pease, C. H., 6 1990. Polynyas and leads: An overview of physical processes and environment. Journal of Geophysical Research: Oceans (19782012) 95 (C6), 9461–9479.

St-Laurent, P., Saucier, F. J., Dumais, J.-F., 2008. On the modification of tides in a seasonally ice-covered sea. Journal of Geophysical Research: Oceans 113 (C11), c11014.

Stammer, D., Ray, R. D., Andersen, O. B., Arbic, B. K., Bosch, W., Carrère, L., Cheng, Y., Chinn, D. S., Dushaw, B. D., Egbert, G. D., Erofeeva, S. Y., Fok, H. S., Green, J. A. M., Griffiths, S., King, M. A., Lapin, V., Lemoine, F. G., Luthcke, S. B., Lyard, F., Morison, J., Müller, M., Padman, L., Richman, J. G., Shriver, J. F., Shum, C. K., Taguchi, E., Yi, Y., 2014. Accuracy assessment of global barotropic ocean tide models. Reviews of Geophysics 52 (3), 243–282.

Stroeve, J., Holland, M. M., Meier, W., Scambos, T., Serreze, M., 2007. Arctic sea ice decline: Faster than forecast. Geophysical Research Letters 34 (9), l09501.

Tait, B. J., Grant, S. T., St.-Jacques, D., Stephenson, F., 1986. Canadian Arctic tide measurement techniques and results. International hydrographic review 63, 111–131.

Tang, C., Fissel, D., 1991. A simple ice-ocean coupled model for ice drift in marginal ice zones . Journal of Marine Systems 2 (3-4), 465 – 475.

van Scheltinga, A. D. T., Myers, P. G., Pietrzak, J. D., 2012. Mesh generation in archipelagos. Ocean Dynamics 62 (8), 1217–1228.

Walsh, J. E., Chapman, W. L., Fetterer, F., 2015. Gridded monthly sea ice extent and concentration, 1850 onwards, Version 1.1. Boulder, Colorado USA: National Snow and Ice Data Center. Digital media.
URL http://dx.doi.org/10.7265/N5833PZ5

Wang, J., Kwok, R., Saucier, F. J., Hutchings, J., Ikeda, M., Hibler, W., Haapala, J., Coon, M. D., Meier, H. E. M., Eicken, H., Tanaka, N., Prentki, D., Johnson, W., 2003. Working toward improved small-scale sea ice-ocean modeling in the Arctic seas. Eos, Transactions American Geophysical Union 84 (34), 325–330.

Weatherall, P., Marks, K. M., Jakobsson, M., Schmitt, T., Tani, S., Arndt, J. E., Rovere, M., Chayes, D., Ferrini, V., Wigley, R., 2015. A new digital bathymetric model of the world's oceans. Earth and Space Science 2 (8), 331–345.

Webb, D. J., 2014. On the tides and resonances of Hudson Bay and Hudson Strait. Ocean Science 10 (3), 411–426.

Appendix A. Comparison with the tide gauges

Figures A.17-A.24 show the maps of the computed tidal characteristics together with the amplitude and phase errors at the tide gauge stations. A color scale shown to the left of every figure refers to the amplitude/phase range of the tidal constituents. The absolute amplitude/phase error values are shown by means of triangular markers colored according to the color scale on the figure's right. A triangle pointing upward indicates that the observed amplitude/phase exceeds the modelled value (under-prediction) and a downward pointing triangle indicates that the modelled amplitude/phase exceeds the observed one (over-prediction).

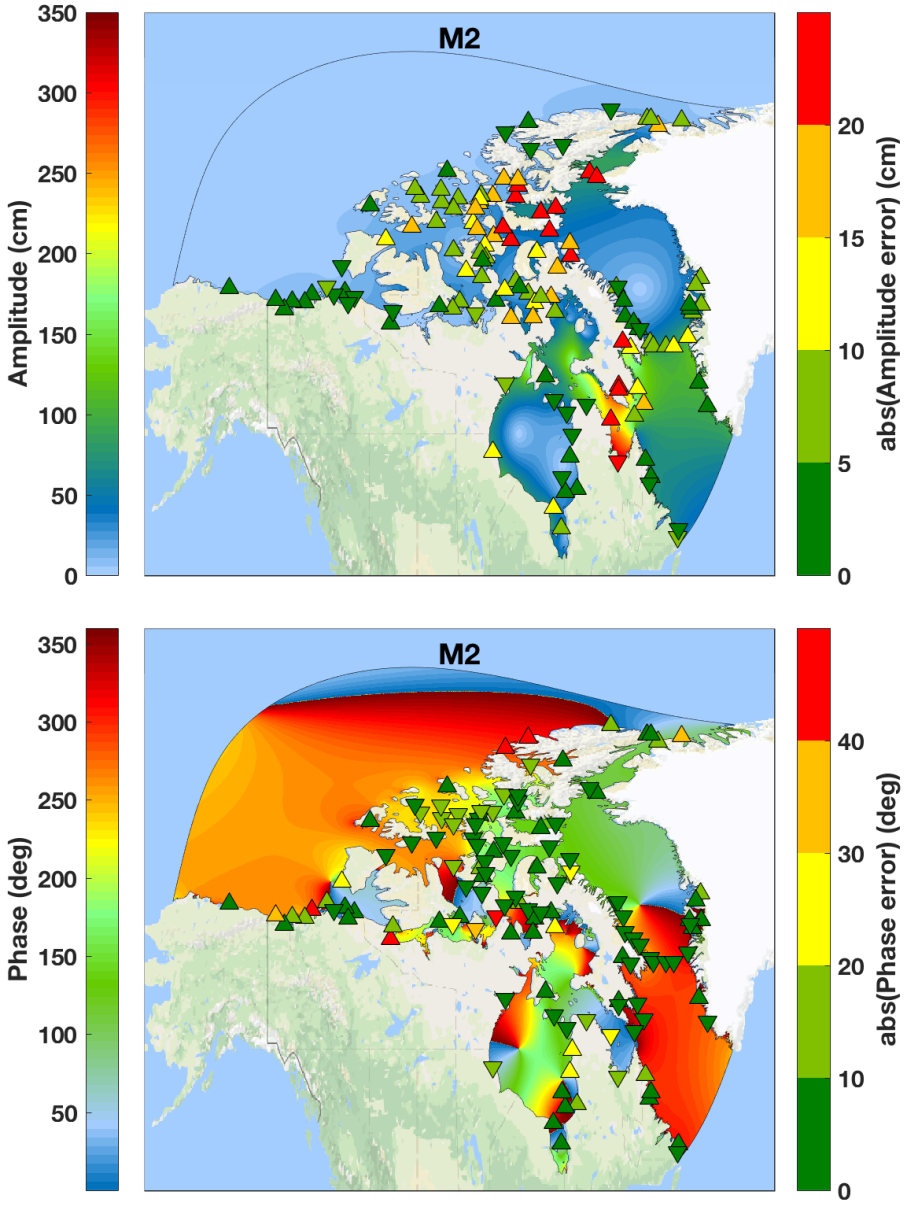

Figure A.17: Computed annual mean characteristics of the M2 tidal constituent together with the amplitude and phase errors at the tide gauge stations. The left color scale shows amplitude/phase range, the right one shows absolute value of the amplitude/phase error at the stations. A triangle pointing upward/downward indicates under-prediction/over-prediction.

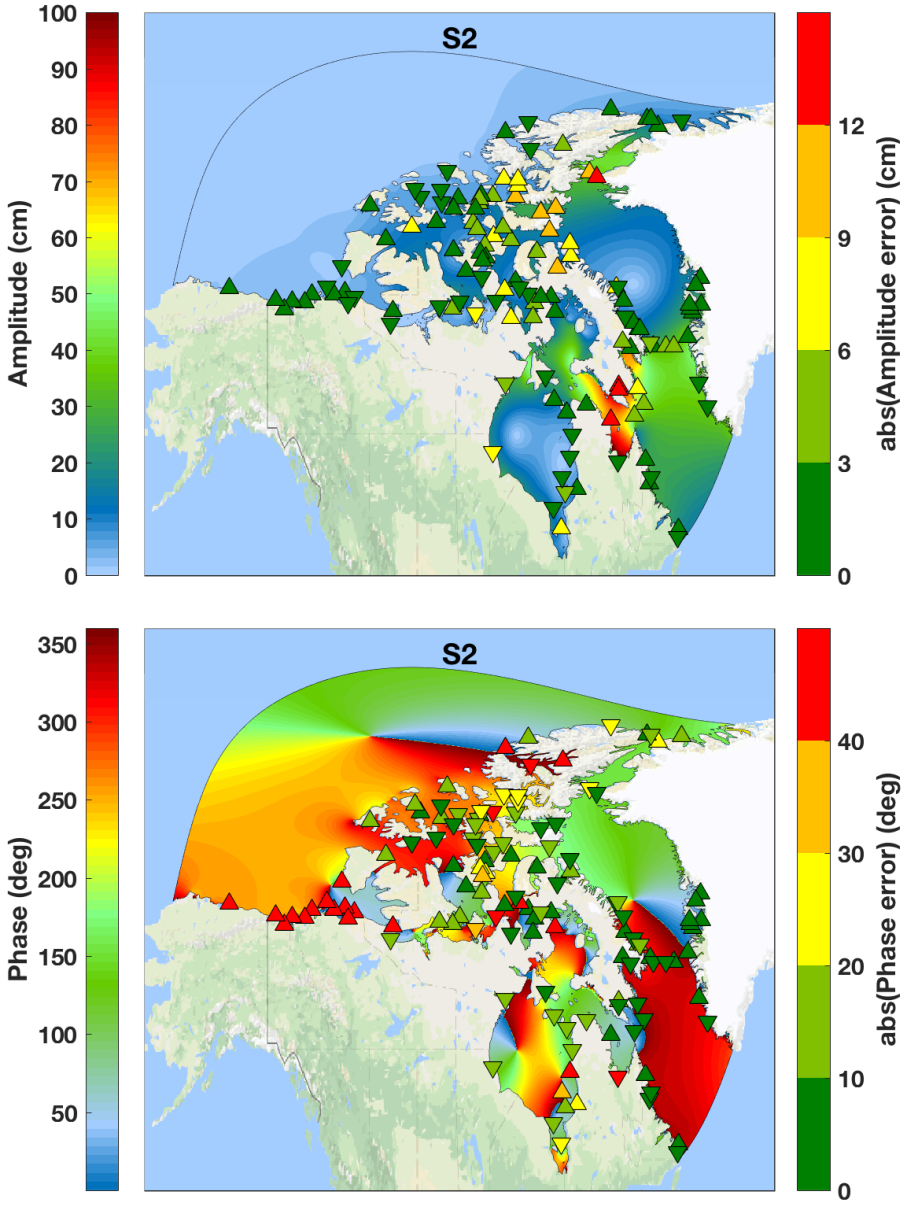

Figure A.18: Computed annual mean characteristics of the S2 tidal constituent together with the amplitude and phase errors at the tide gauge stations. The left color scale shows amplitude/phase range, the right one shows absolute value of the amplitude/phase error at the stations. A triangle pointing upward/downward indicates under-prediction/over-prediction.

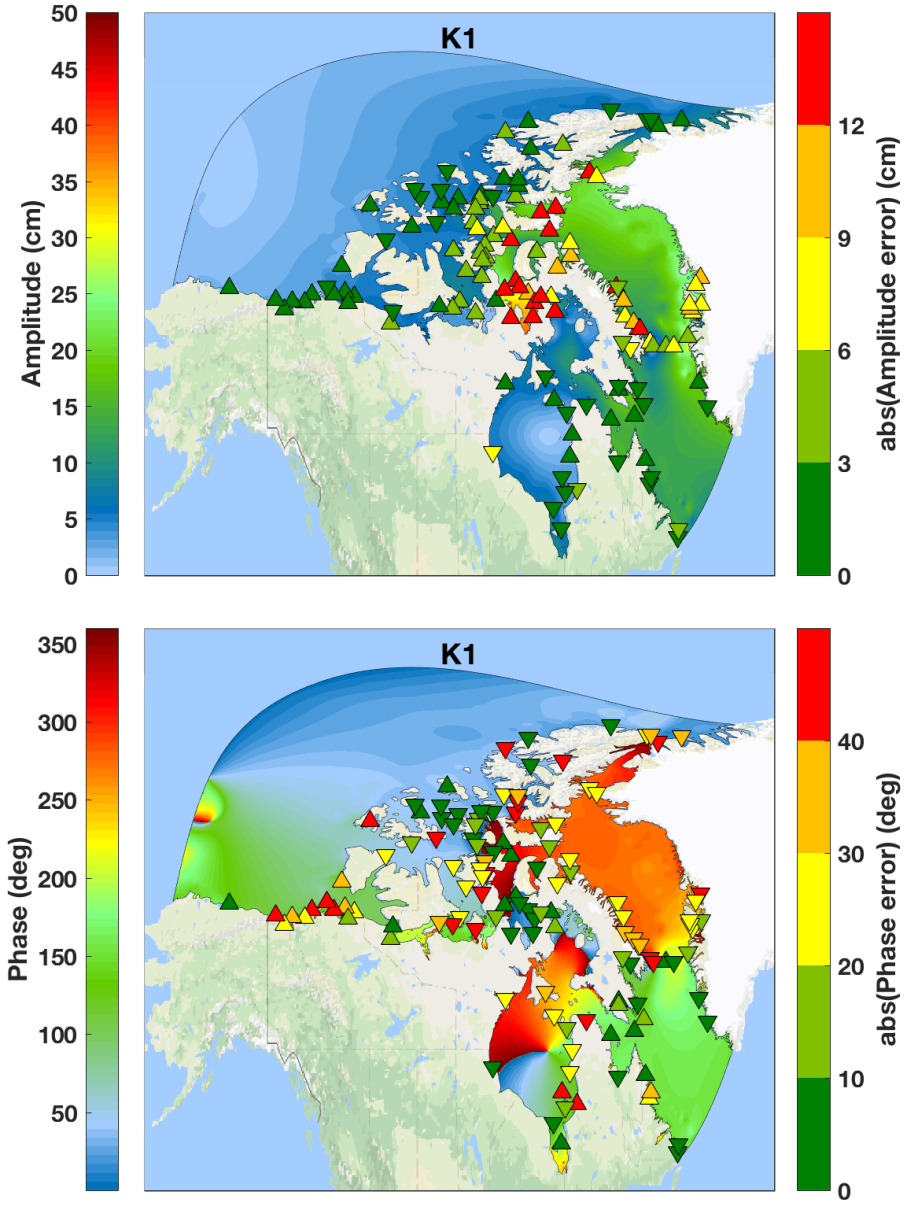

Figure A.19: Computed annual mean characteristics of the K1 tidal constituent together with the amplitude and phase errors at the tide gauge stations. The left color scale shows amplitude/phase range, the right one shows absolute value of the amplitude/phase error at the stations. A triangle pointing upward/downward indicates under-prediction/over-prediction.

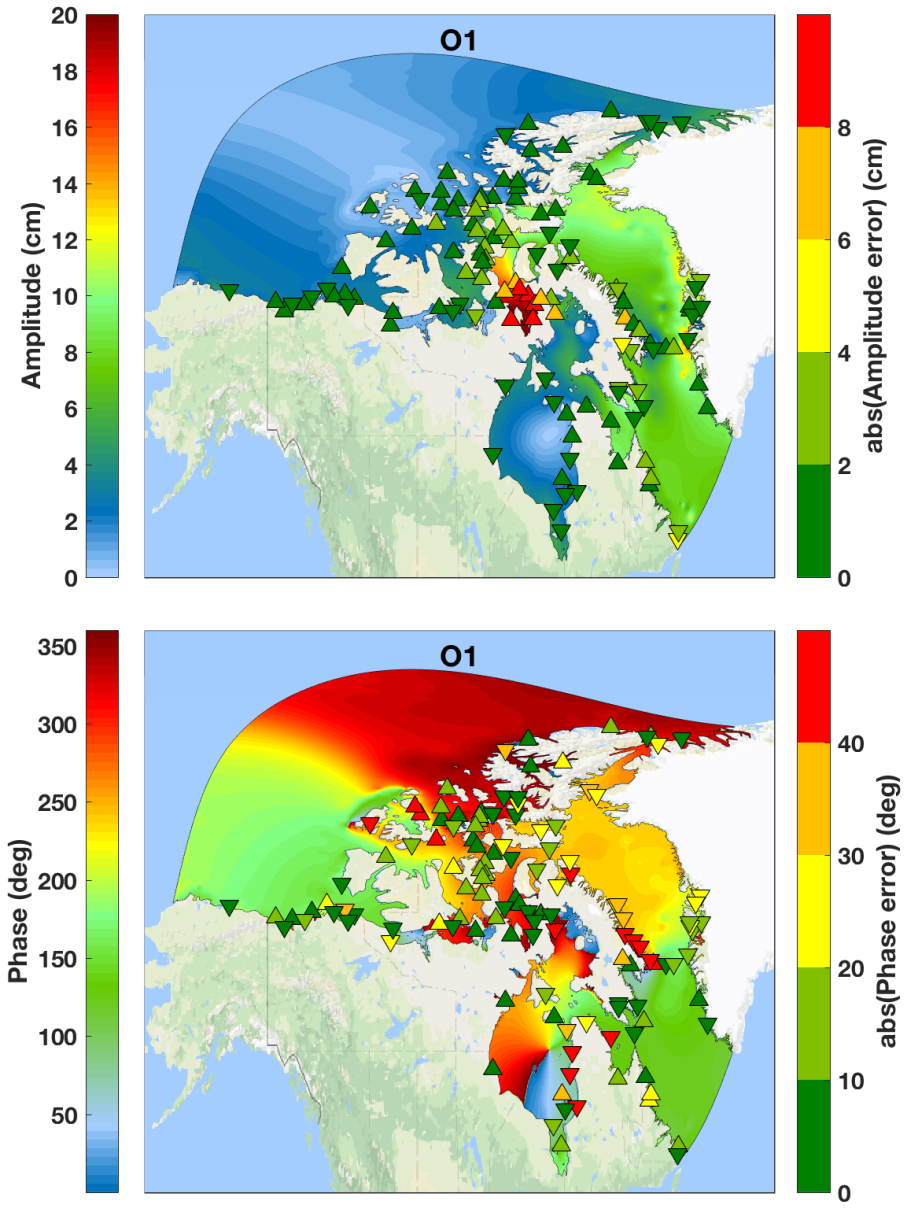

Figure A.20: Computed annual mean characteristics of the O1 tidal constituent together with the amplitude and phase errors at the tide gauge stations. The left color scale shows amplitude/phase range, the right one shows absolute value of the amplitude/phase error at the stations. A triangle pointing upward/downward indicates under-prediction/over-prediction.

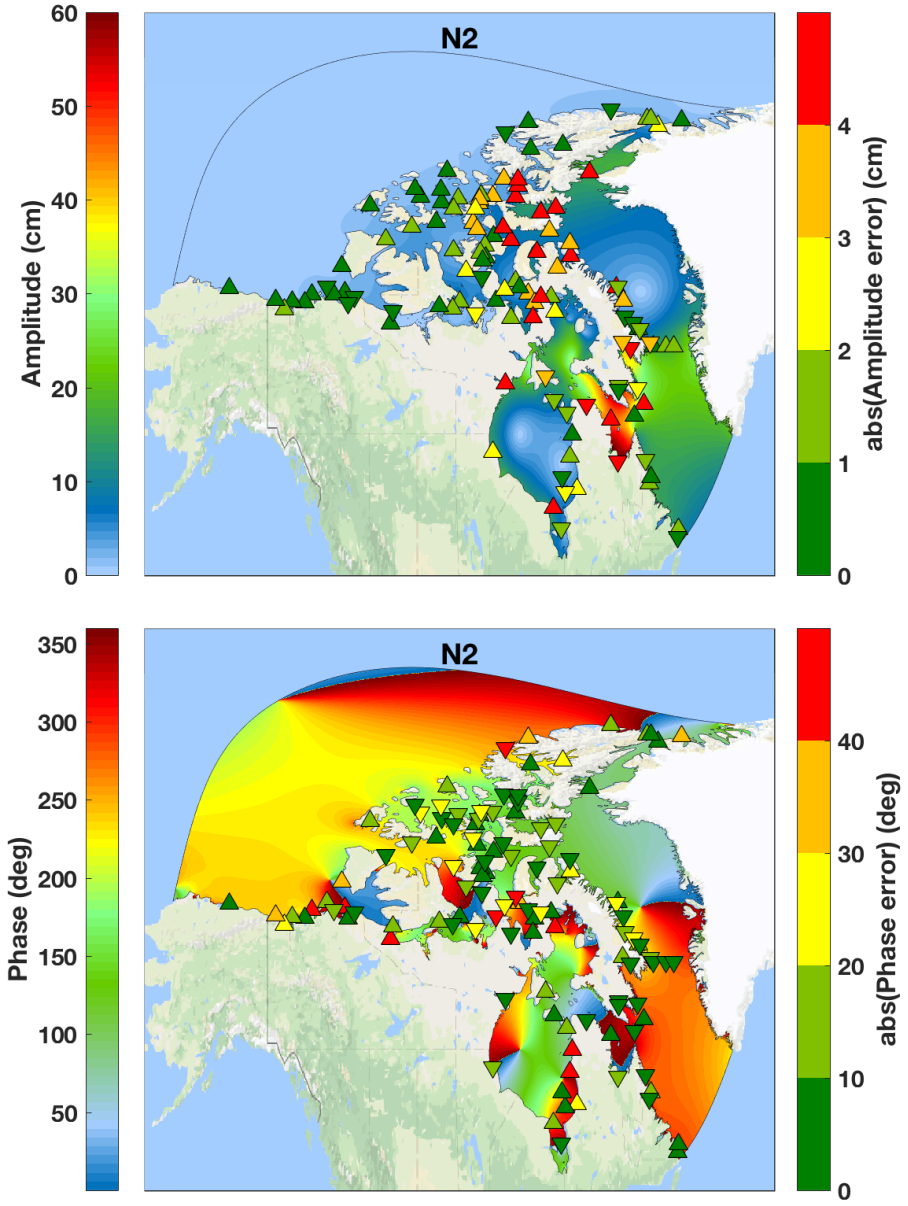

Figure A.21: Computed annual mean characteristics of the N2 tidal constituent together with the amplitude and phase errors at the tide gauge stations. The left color scale shows amplitude/phase range, the right one shows absolute value of the amplitude/phase error at the stations. A triangle pointing upward/downward indicates under-prediction/over-prediction.

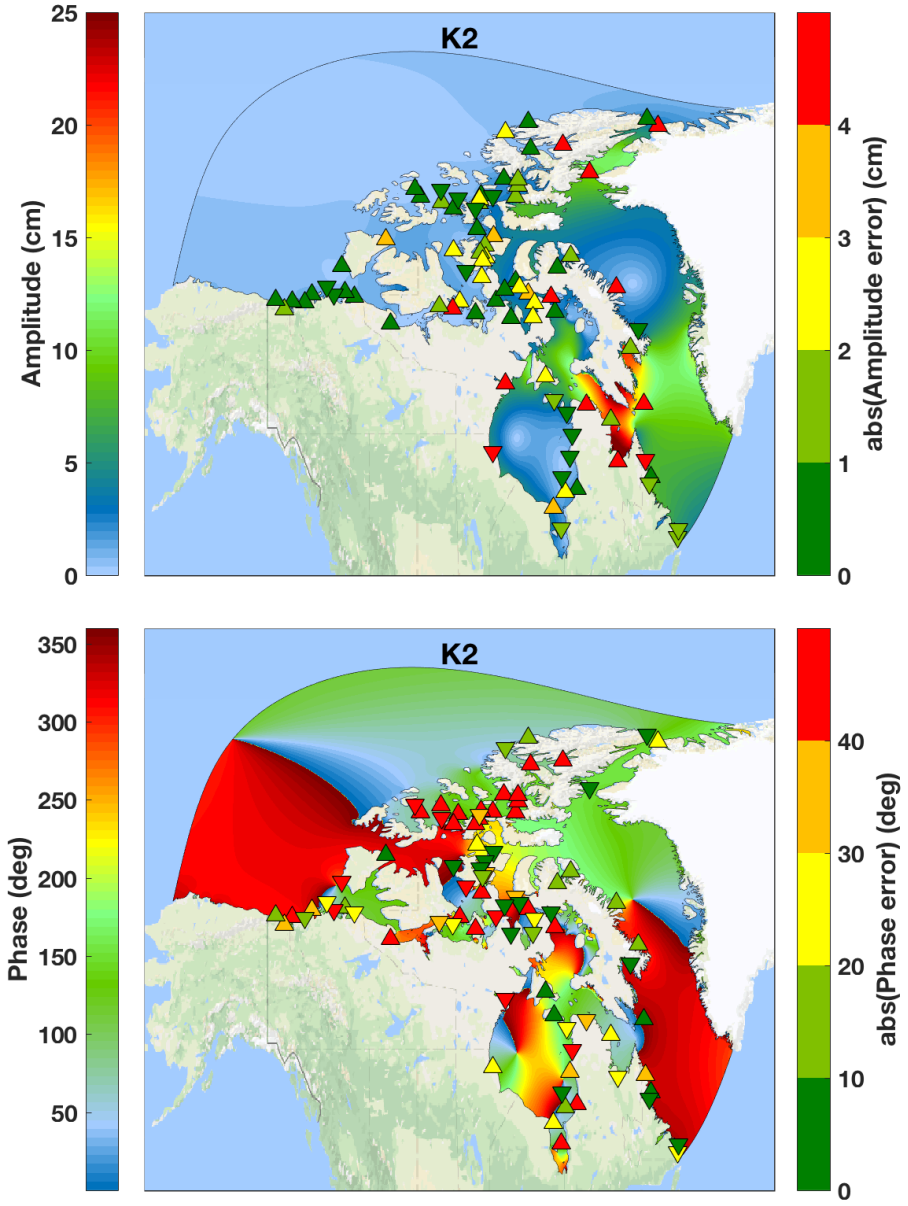

Figure A.22: Computed annual mean characteristics of the K2 tidal constituent together with the amplitude and phase errors at the tide gauge stations. The left color scale shows amplitude/phase range, the right one shows absolute value of the amplitude/phase error at the stations. A triangle pointing upward/downward indicates under-prediction/over-prediction.

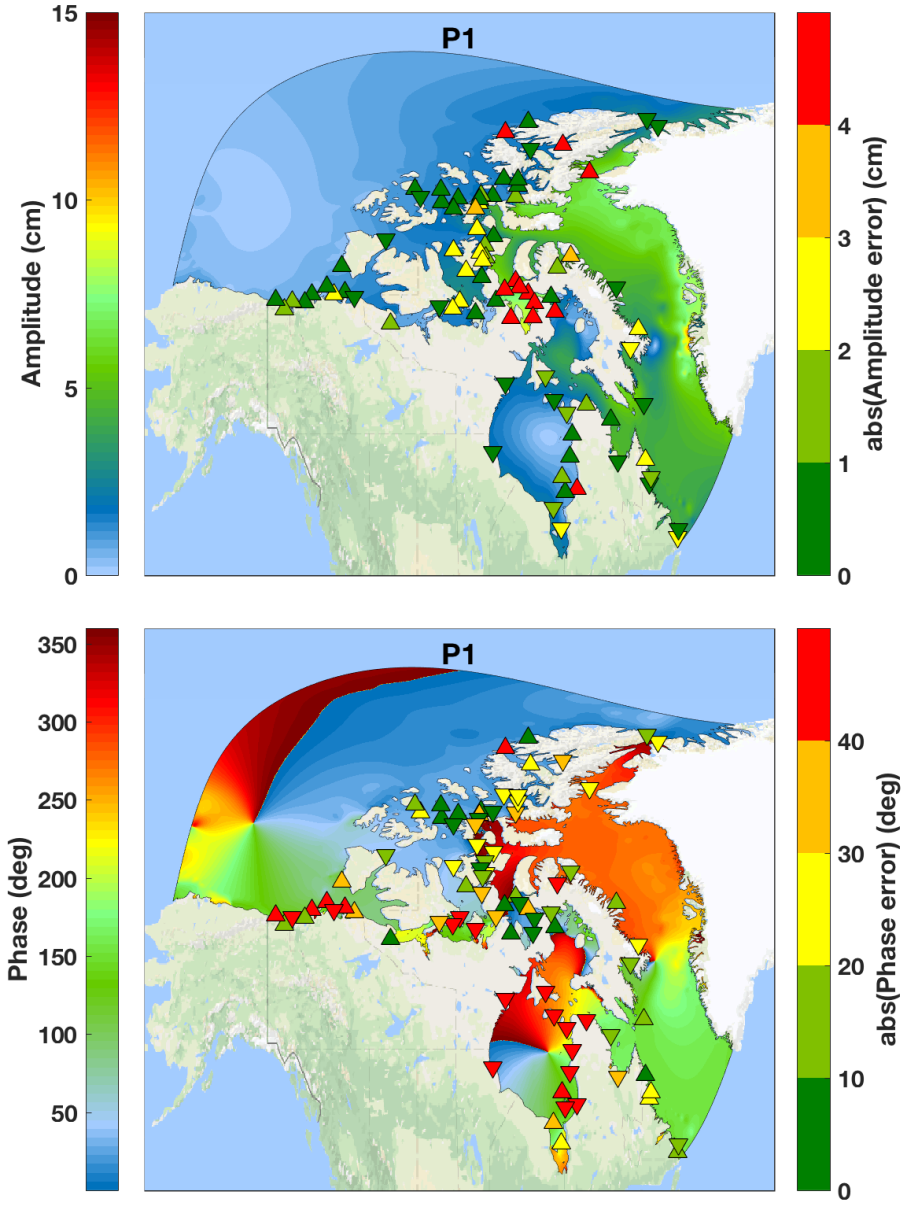

Figure A.23: Computed annual mean characteristics of the P1 tidal constituent together with the amplitude and phase errors at the tide gauge stations. The left color scale shows amplitude/phase range, the right one shows absolute value of the amplitude/phase error at the stations. A triangle pointing upward/downward indicates under-prediction/over-prediction.

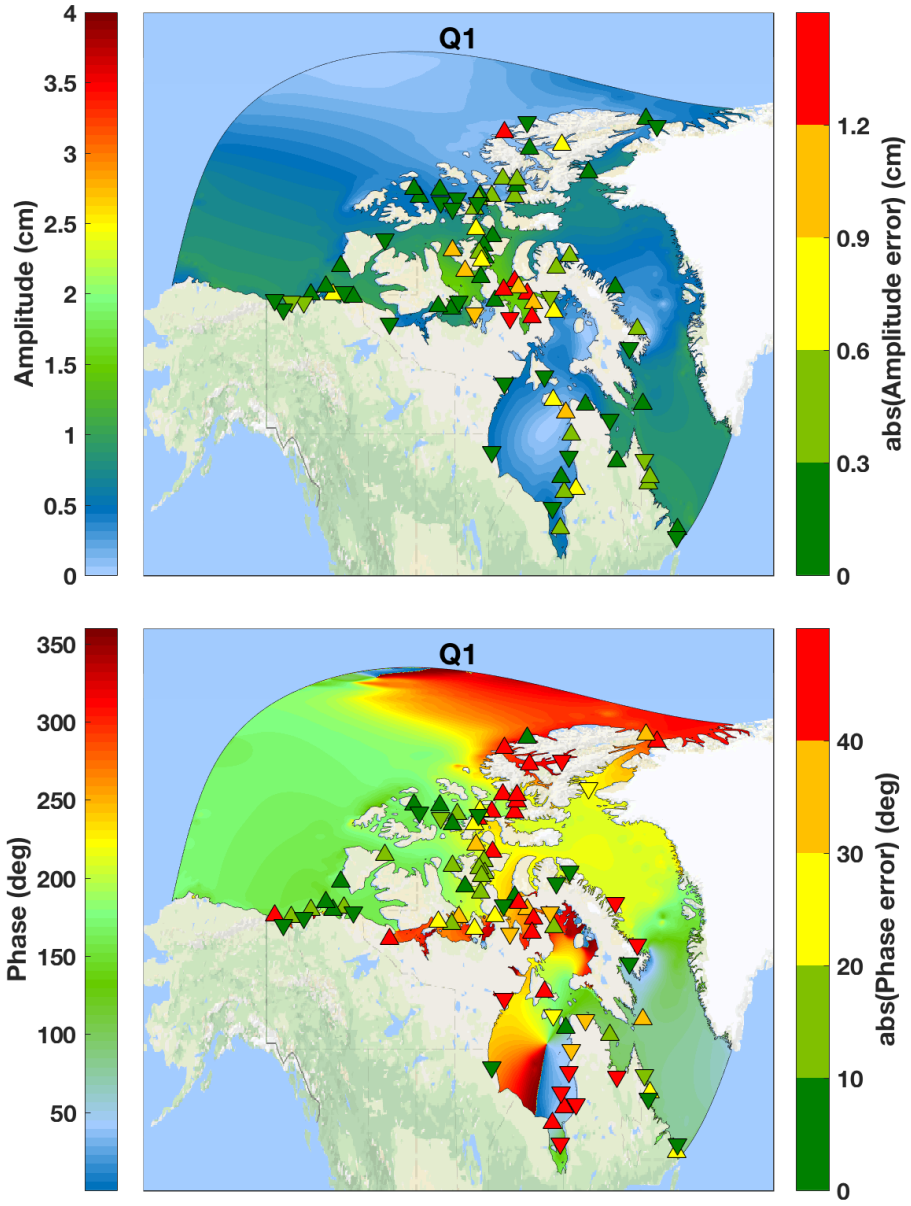

Figure A.24: Computed annual mean characteristics of the Q1 tidal constituent together with the amplitude and phase errors at the tide gauge stations. The left color scale shows amplitude/phase range, the right one shows absolute value of the amplitude/phase error at the stations. A triangle pointing upward/downward indicates under-prediction/over-prediction.

Appendix B. Ice induced variability of tidal constants: comparison to observations

To assess ability of the model to reproduce seasonality of the tidal constants, a number of tide gauges with records spanning multiple years were selected. The approximate locations of the tide gauges are shown in Figure B.25. Monthly elevations

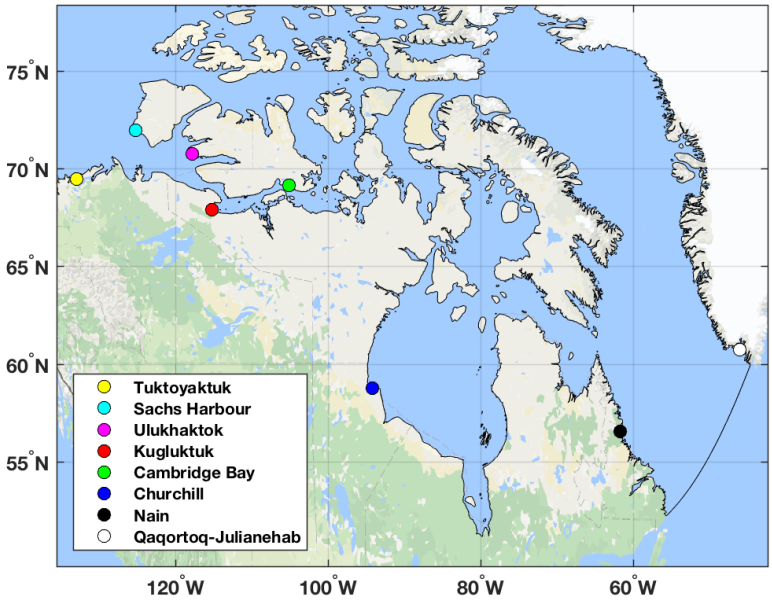

Figure B.25: Tide gauges used for evaluation of seasonal cycle

of M2 tide obtained from the tide gauge records are plotted against the model results in Figure B.26. Here we used two different values for the ice drag coefficient defined in Equation (2). Namely, $C_{D_{ice}} = 1.8 * 10^{-2}$, the value used throughout this paper (dashed line) and $C_{D_{ice}} = 2.5 * 10^{-3}$ as typically used in global tidal models for the fast ice cells (dotted line). In all cases the amplitude anomaly is shown relative to September.

The temporal variability of the M2 amplitude at the four most western stations is reproduced by the model reasonably well when the higher value of the ice drag coefficient is used. There is, however, slight shift in the phase of the modulation for Sachs Harbor and Ulukhaktok stations. The amplitude variations at the Cambridge Bay are underestimated in both the cases, whereas at the remaining stations it is highly overestimated.

The ice-ocean drag coefficient is determined as a function of the undersurface sea ice roughness length. Since under-surface sea ice roughness can vary considerably according to the estimation method and the level of the sea ice deformation, so does the calculated drag coefficient. The estimated value typically ranges from 1.32×10^{-3} to

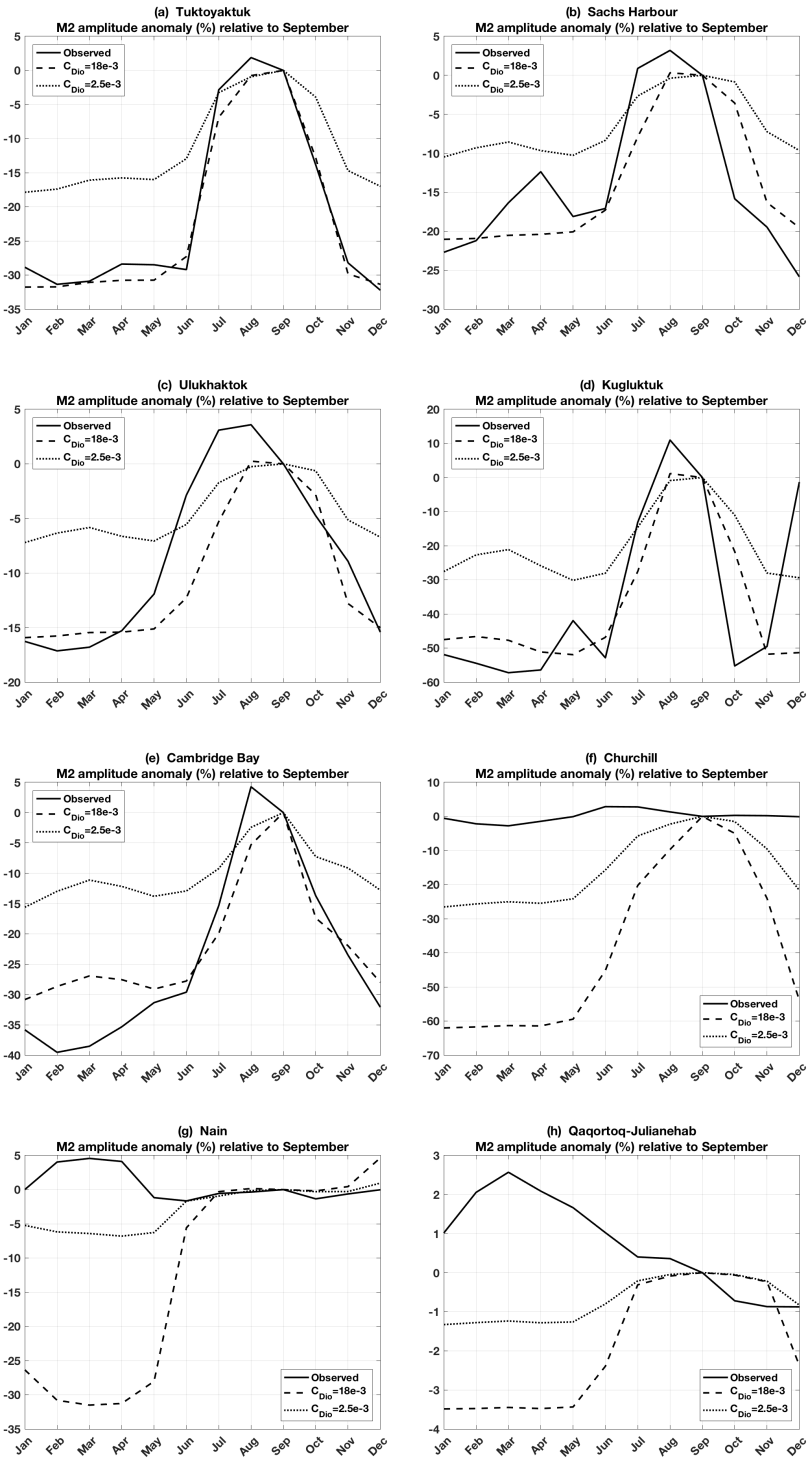

Figure B.26: Monthly amplitude anomaly of the M2 tidal constituent from observations (solid line), and the experiments with different values of ice-ocean drag coefficient. All values are referenced to those in September.

26.8×10^{-3}, see for example Pease et al. (1983); Langleben (1982); Madsen and Bruno (1987). Moreover, the aerodynamic properties of the ice cover change seasonally due to growth and decay. For the numerical model, however, a single value of the ice-ocean drag coefficient is chosen by the modeler and is kept constant for the entire duration of the simulation. A possibility to include space and time varying ice-ocean drag coefficient requires additional research.

Appendix C. Decadal scale variations of the ice induced tidal seasonality

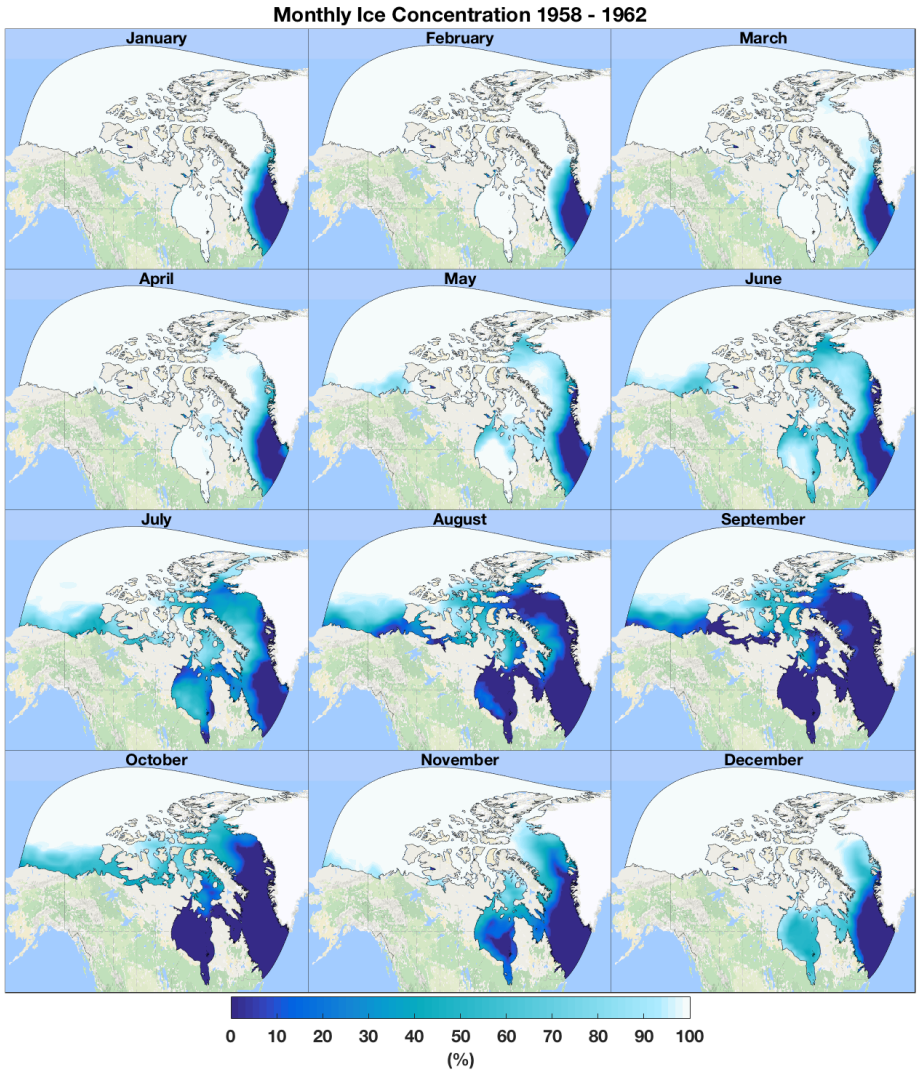

Figure C.27: Monthly 1958-1962 median sea ice concentration, Walsh et al. (2015).

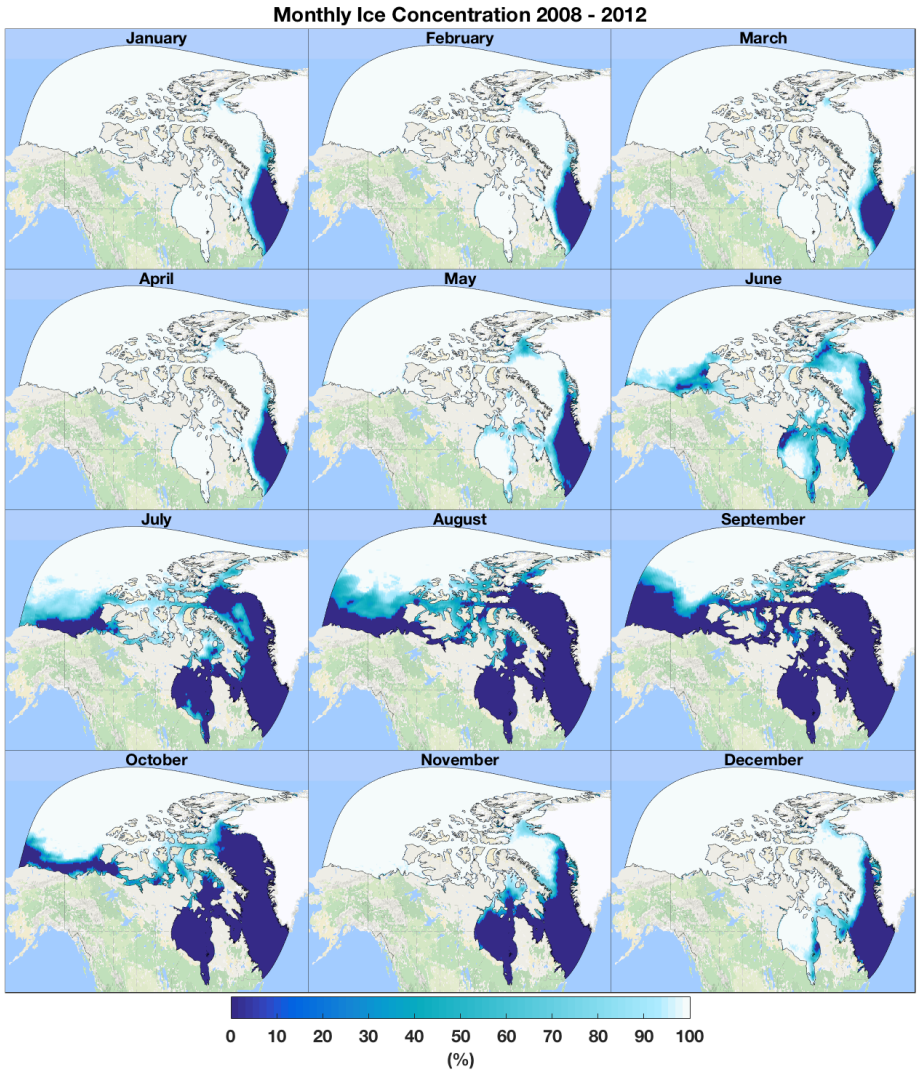

Figure C.28: Monthly 2008-2012 median sea ice concentration, Walsh et al. (2015).

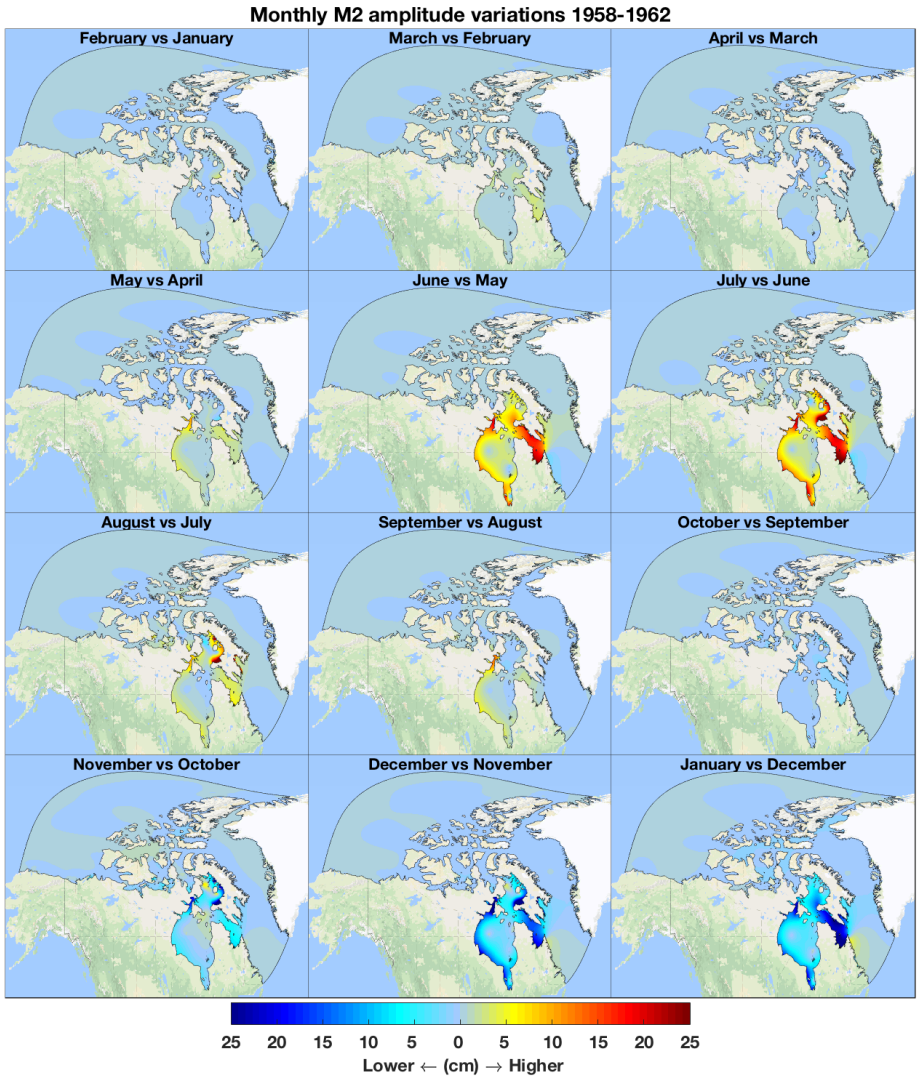

Figure C.29: Monthly amplitude variations of M2 tidal constituent during the period from 1958 to 1962. Yellow/red colors indicate increase in amplitude with respect to the previous month.

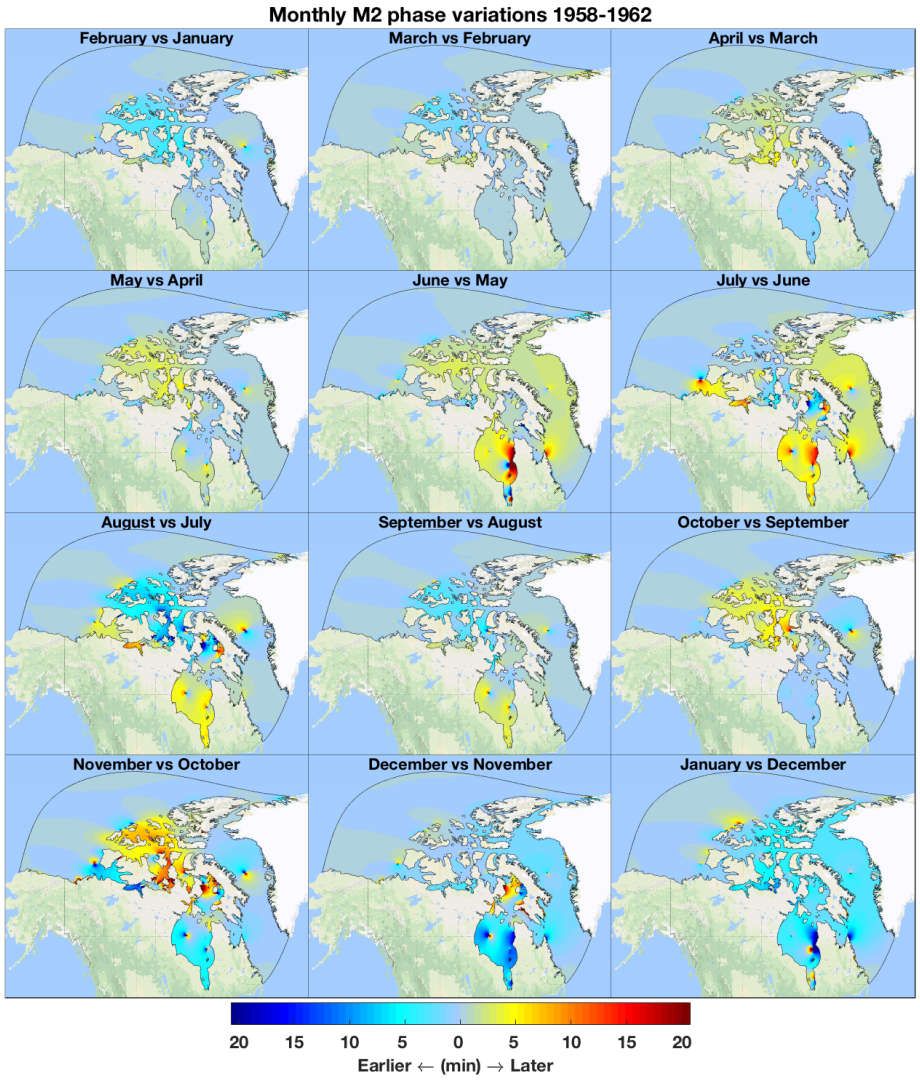

Figure C.30: Monthly phase variations of M2 tidal constituent during the period from 1958 to 1962. Yellow/red colors indicate later arrival compared to the previous month.

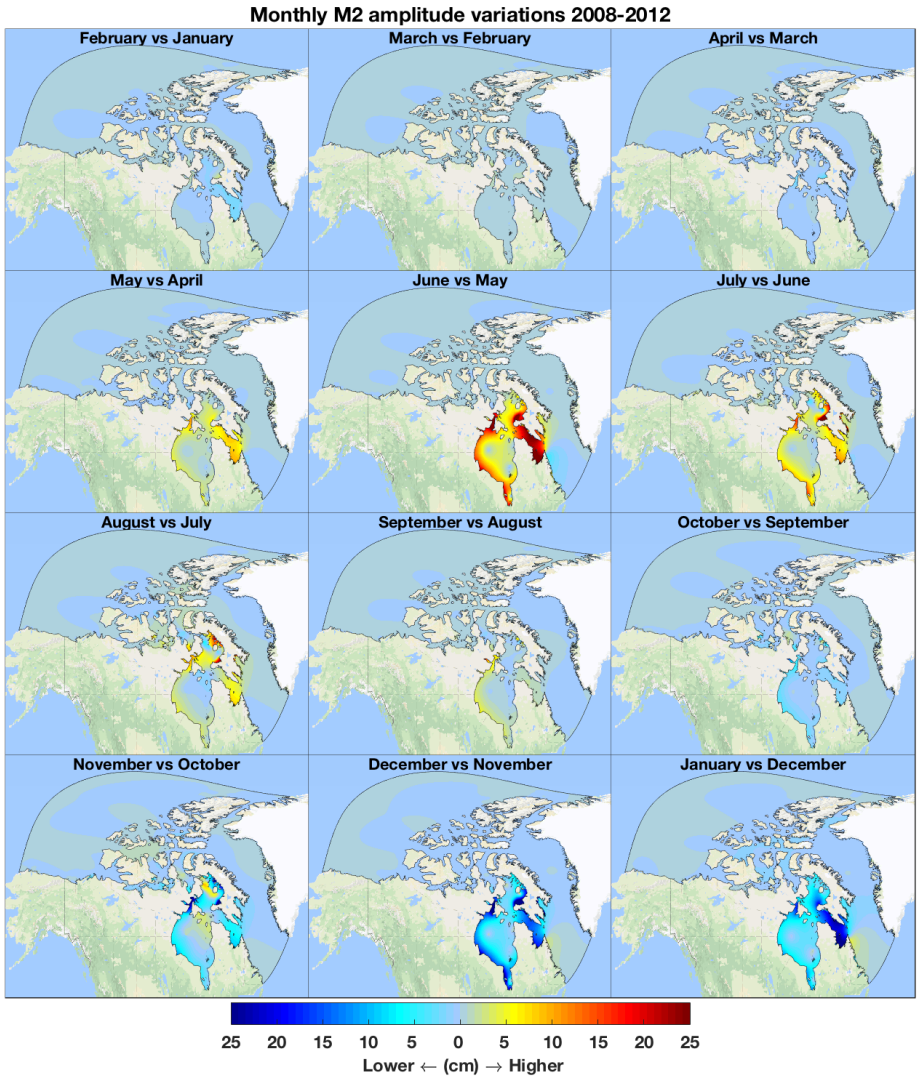

Figure C.31: Monthly amplitude variations of M2 tidal constituent during the period from 2008 to 2012. Yellow/red colors indicate increase in amplitude with respect to the previous month.

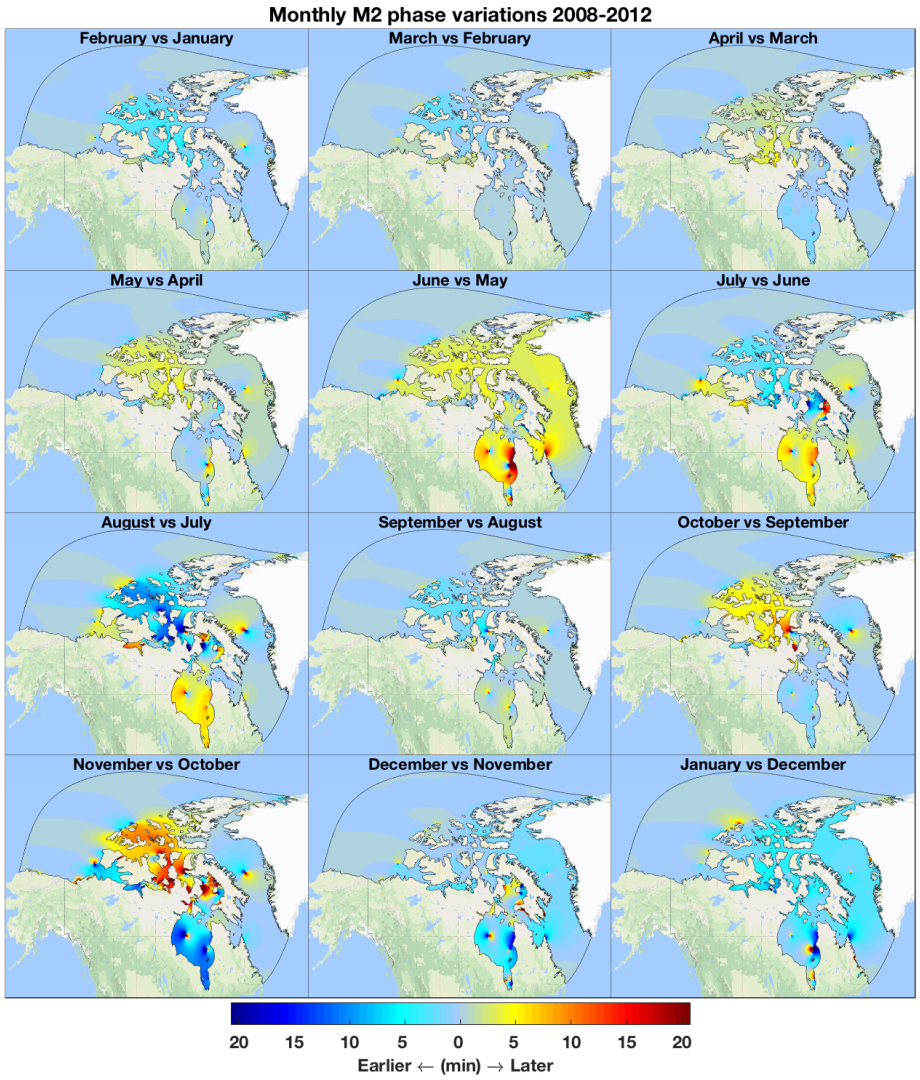

Figure C.32: Monthly phase variations of M2 tidal constituent during the period from 2008 to 2012. Yellow/red colors indicate later arrival compared to the previous month.